Implementation of WRF-Urban Asymmetric Convective Model (UACM) for Simulating Urban Fog over Delhi, India

Utkarsh Prakash Bhautmage[1*], Sachin D. Ghude[1*], Avinash N. Parde[1,2], Harsh G. Kamath[5], Narendra Gokul Dhangar[1], Jonathan Pleim[3], Michael Mau Fung Wong[4], Sandeep Wagh[1], Rakesh Kumar[6], Dev Niyogi[5], M. Rajeevan[7]

[1]Indian Institute of Tropical Meteorology, Ministry of Earth Sciences (MoES), Pashan, Pune, India.

[2]Department Atmospheric and Space Sciences, Savitribai Phule Pune University, Pune, India.

[3]Atmospheric & Environmental Systems Modeling Division, CEMM/ORD/USEPA, Research Triangle Park, NC, USA.

[4]Division of Environment and Sustainability, Hong Kong University of Science and Technology, Hong Kong, China.

[5]Department of Earth and Planetary Sciences, Jackson School of Geosciences, The University of Texas at Austin, Austin, TX 78712, USA.

[6]India Meteorological Department, New Delhi, India.

[7]Ministry of Earth Sciences, New Delhi, India.

*Corresponding authors: Utkarsh Prakash Bhautmage (upbhautmage@connect.ust.hk),

Sachin D. Ghude (sachinghude@tropmet res.in)

† Indian Institute of Tropical Meteorology, Pashan, Pune, India.

Key Points:

1. The new multilayer WRF-UACM, explicitly incorporating urban physics and morphology, is implemented to simulate fog over the Delhi region.
2. Improvements in the prediction of urban wind, temperature, and relative humidity are demonstrated using UACM on fog days and clear skies.
3. Abilities of novel UACM in capturing urban fog phenomena along with its operational mode capabilities over the Delhi region are examined.

Abstract

Accurate fog prediction in densely urbanized cities poses a challenge due to the complex influence of urban morphology on meteorological conditions in the urban roughness sublayer. This study implemented a coupled WRF-Urban Asymmetric Convective Model (WRF-UACM) for Delhi, India, integrating explicit urban physics with Sentinel-updated USGS land-use and urban morphological parameters derived from the UT-GLOBUS dataset. When evaluated against the baseline Asymmetric Convective Model (WRF-BACM) using Winter Fog Experiment (WiFEX) data, WRF-UACM significantly improved urban meteorological variables like diurnal variation of 10-meter wind speed, 2-meter air temperature (T2), and 2-meter relative humidity (RH2) on a fog day. UACM also demonstrates improved accuracy in simulating temperature and a significant reduction in biases for RH2 and wind speed under clear sky conditions. UACM reproduced the nighttime urban heat island effect within the city, showing realistic diurnal heating and cooling patterns that are important for accurate fog onset and duration. UACM effectively predicts the onset, evolution, and dissipation of fog, aligning well with observed data and satellite imagery. Compared to WRF-BACM, WRF-UACM reduces the cold bias soon after the sunset, thus improving the fog onset error by ~4 hours. This study underscores the UACM's potential in enhancing fog prediction, urging further exploration of various fog types and its application in operational settings, thus offering invaluable insights for preventive measures and mitigating disruptions in urban regions.

Plain Language Summary

In Delhi, accurately predicting fog in urban areas is difficult due to complex factors like city layout and infrastructure. This study employed the recently developed WRF-UACM with detailed UT-GLOBUS urban morphological parameters for fog simulation. Compared to existing models, WRF-UACM predicted wind, temperature, and humidity better under both clear skies and foggy conditions. Our model accurately reproduced urban warming and cooling patterns that are crucial for fog prediction and urban meteorology. WRF-UACM improves the diurnal variation of winds and reduces temperature cold bias after the sunset, thus improving fog onset by ~4 hours. This work highlights the potential of WRF-UACM for fog prediction and offers valuable insights for urban meteorology.

Keywords:

Boundary layer meteorology, Urban canopy parameterization, Urban morphological parameters, Urban heat island, WRF model, Fog

1. Introduction

In the densely populated Indo-Gangetic Plains (IGP), the winter season ushers in frequent and widespread fog occurrences (Bhushan et al., 2003; Singh and Kant, 2006; Gautam et al., 2007; Ghude et al., 2017). These fog episodes drastically reduce visibility to just a few tens of meters, disrupting transportation and impacting the lives of millions of inhabitants. Radiation fog, a prevalent type in this region (Singh and Kant, 2006; Singh et al. 2007; Ghude et al., 2023), has exhibited significant spatiotemporal variability due to the complex terrain of the area, including urbanization over the past two decades (Sawaisarje et al., 2014; Singh and Gautam, 2022; Parde et al., 2023). Rapid urbanization leads to changes in local climate and conducive fog meteorology, resulting in "urban fog" (Sachweh and Koepke, 1997). Urbanization disrupts natural temperature, humidity, aerosol loading and wind circulation, leading to the genesis of an "urban heat island" (UHI) that is often characterized by higher land surface and air temperatures in cities compared to surrounding rural areas (AMS Glossary, 2020). As urban areas in the IGP, particularly Delhi region, continue to sprawl, there is a corresponding rise in the occurrence of fog "holes" or patches that tend to dissipate at an earlier stage (Gautam & Singh, 2018). Considering the future, climate change could lead to more frequent episodes of widespread fog over the IGP in winter, except in areas where air pollution and greenhouse warming effects outweigh the fog formation (Hingmire et al., 2021). Recent research by Gu et al. (2019) and Hingmire et al. (2021) has revealed a decrease in fog events over urbanized regions of Shanghai and the North India over the past recent years. This decline is mainly attributed to the urban heat island (UHI) effect resulting from changes in land use and surface properties. Gautam and Singh (2018) and other sources have reported that the UHI effect leads to higher surface temperatures and reduced relative humidity, resulting in decreased condensation and, consequently, reduced fog formation.

Globally, radiation fog events, including those in Delhi, pose challenges for Numerical Weather Prediction (NWP) models to simulate and predict (Pithani et al., 2020; Jaykumar et al., 2021; Parde et al., 2022a). Various factors contribute to the complexity of fog, including the boundary layer phenomenon, which may involve interactions between air masses with different temperatures and moisture content, meteorological field-variables' variations, interactions between atmospheric flow and complex landscapes, large-scale synoptic motions, and the impact

of aerosol loading in the shallow boundary layer (Bhowmik et al., 2004; Jenamani et al., 2007; Sawaisarje et al., 2014; Ghude et al., 2017, 2023; Hingmire et al., 2019; Dhangar et al., 2021, 2022; Gunturu and Kumar, 2021). Accurately predicting fog through the present numerical models remains a formidable challenge. Typically, individual model forecasts tend to exhibit a noticeable bias in the onset and dissipation timing of fog (Bhowmik et al., 2004; Jayakumar et al., 2018; Pithani et al., 2020; Wagh et al., 2023; Yadav et al., 2022). However, a recently introduced ensemble fog forecasting approach (utilizing the ensembles of multiple initial conditions or models or physics) proves to be more effective than single-model-based forecasts in addressing the biases related to fog onset and dissipation (Zhou and Du, 2010; Price et al., 2015; Pahlavan et al., 2021; Parde et al., 2022a). Nevertheless, it's important to note that this ensemble-based approach comes with increased computational costs. While data assimilation has the potential to address several issues in fog forecasting that stem from errors in the initial conditions of land-surface fields (e.g. soil moisture and temperature) and atmospheric states, persistent challenges remain within the models for fog prediction, including large onset errors, diurnal bias in 2-meter temperature due to rapid warming(cooling) during day(night), in 10-meter wind speed, and over-prediction of liquid water content (LWC) within the fog layers as well as bias in their vertical extents (Bari et al., 2023; Bergot and Guedalia, 1994; Ghude et al., 2023; Müller et al., 2007; Rémy et al., 2010; Steeneveld et al., 2015; Gao et al., 2018; Pithani et al., 2020; Parde et al., 2022b). Furthermore, urban warming frequently disrupts boundary layer stability, the inversion layer, and diminishes liquid droplets due to reduced condensation in urban locales, thereby hindering the genesis of radiation fog (Gu et al., 2019). The large-eddy simulation study at Paris–Charles de Gaulle airport by Bergot et al. (2015) emphasizes the critical importance of incorporating comprehensive building representations to enhance the precision of local radiation fog forecasts. This underscores the necessity of considering small-scale variations within the urban canopy to advance the accuracy of fog predictions. However, the presently available operational fog forecasting models, especially in India, lack consideration for detailed urban morphology representation and realistic UHI effect. This has resulted in reduced forecasting accuracy and an increased likelihood of false alarm ratio (Pithani et al., 2020; Parde et al., 2022a). In essence, these investigations highlight the significance of adopting advanced numerical modeling methods to inform efficient fog adaptation strategies in cities.

The study conducted by Theethai Jacob et al. (2023) involved the integration of a comprehensive urban surface-flux scheme into a high-resolution Delhi Model with Chemistry and aerosol framework (DM-Chem), utilizing urban morphology data specific to the Delhi region obtained from empirical relationships. Their aim was to simulate the UHI and urban cool island (UCI) effects under clear sky and foggy conditions. However, significant biases were identified in the simulation of relative humidity and the underestimation of latent heat flux, particularly during foggy conditions. For precise representation of urban boundary layer, specific urban modeling options have also been integrated into the state-of-the-art Weather Research and Forecasting (WRF) model. These include the single-layer Urban Canopy Model (UCM) (Kusaka et al., 2001), and multi-layer Building Effect Parameterization-Building Energy Model (BEP-BEM) (Martilli et al., 2002; Salamanca & Martilli, 2010). However, these urban models present certain challenges and limitations, particularly when implemented in operational mode (details elaborated in Bhautmage et al., 2022). Notably, a drawback of the renowned BEP-BEM model is its coupling with only a limited set of local planetary boundary layer (PBL) schemes in WRF such as, Mellor-Yamada-Janjic (MYJ) (Janjić, 1994; Mellor & Yamada, 1974, 1982) and Boulac (Bougeault & Lacarrere, 1989), and nonlocal Yonsei University (YSU) scheme (Hong et al., 2006; Hendricks et al., 2020). Furthermore, these models are computationally resource-intensive when operated at higher spatial, vertical, and temporal resolutions (Chen & Dudhia, 2001). Importantly, UCM and BEP-BEM models in WRF can only be coupled with the Noah and Noah-MP land surface models (Chen et al., 2011; Niu et al., 2011). To address these challenges and limitations, a recently developed Urban Asymmetric Convective Model (UACM) was introduced by Dy et al. (2019) and Bhautmage et al. (2022).

The UACM is a multilayer urban model based on a hybrid local and non-local flux PBL scheme. The model can estimate the momentum drag exerted by the building structures on the airflow as well as the thermal and moisture fluxes evolving from the urban facets. The urban morphological parameters play a vital role in simulating the meteorological conditions and field variable magnitudes within the urban roughness sublayer in the UACM. The model has shown significant improvement in simulating the wind speed and temperature when implemented over the dense-urbanized Pearl River Delta (PRD) economic region in Southern China (Bhautmage et al., 2022). The UACM demonstrates improved urban 10-meter wind speeds (WS10) by generating sufficient momentum drag, and 2-meter temperatures (T2) by considering the daytime

storage of solar thermal energy within urban structures, and its subsequent release in the nighttime. This extends to the precise modeling of vertical profiles of horizontal wind speeds and temperatures within the urban canopy layer and up to the PBL depth. The model also improves the 2-meter total moisture content and its diurnal trend in urban areas. Furthermore, UACM effectively captures the nocturnal UHI effect by efficiently releasing the daytime stored heat back into the atmosphere. In comparison to alternative urban models, UACM excels in computational efficiency, rendering it well-suited for operational forecasting. More comprehensive insights into the UACM, including its integration with the WRF Version 3.8 (V3.8) model are described in Dy et al. (2019) and Bhautmage et al. (2022).

In this study, we have implemented the WRF-UACM over the urban areas in Delhi region, aiming to simulate scenarios of both the radiation fog event and clear sky day. To enhance the model's accuracy, we have incorporated the most up-to-date United States Geological Survey (USGS) land use data over the Delhi region updated from European Space Agency (ESA) World-Cover 2021 (https://worldcover2021.esa.int) Sentinel satellite observations (Van De Kerchove et al., 2021) as well as high-resolution urban morphological parameters over Delhi derived from the UT-GLOBUS (Kamath et al., 2022). The article is structured as: Section 2 provides comprehensive details about the model framework, urban morphological data, observational sites and data, and case studies specifics. In Section 3, we discussed the research findings for fog and clear sky episodes from both modeling and observational perspectives. Finally, the study concludes with a summary in Section 4.

2. Datasets and Methodology

2.1 Urban Asymmetric Convective Model (UACM) Framework

In this study, the non-hydrostatic mesoscale WRF V3.8 is utilized. This model is fully compressible and utilizes a terrain-following vertical coordinate system. WRF incorporates various physics scheme options for cloud/precipitation microphysics, cumulus convection, PBL, land surface, and shortwave and longwave radiation. These options vary in complexity to accurately simulate atmospheric processes across various spatial scales and regions (Skamarock et al., 2008).

To simulate the urban boundary layer processes, the UACM (Dy et al., 2019; Bhautmage et al., 2022) within WRF has been implemented. The UACM incorporates innovative urban physics through a hybrid local and non-local flux mixing PBL scheme, seamlessly integrated with the modified Pleim-Xiu (PX) land surface model (LSM). This integration effectively addresses urban sensible and latent heat fluxes, alongside momentum fluxes. The UACM is a multilayer urban model that accommodates intricate street canyon geometry and can ingest various urban morphological parameter datasets, including street canyon orientation. All these derived morphological parameters are comprehensively explained in section 2.2. The UACM employs a two-layer force-restore algorithm to estimate urban surface temperatures across the ground, walls, and roofs. These estimations incorporate urban morphological parameters that play a vital role in estimating the amount of radiation reaching urban surfaces, accounting for canyon orientations and dynamic solar zenith angle across diurnal and seasonal cycles. Notably, the model includes momentum drag induced by all three urban surfaces (street, walls, and roof) to simulate wind velocity within the urban canopy (Bhautmage et al., 2022).

In the present work, the WRF-UACM model was configured over the Delhi region, specifically centered on the urbanized expanse of the Delhi-National Capital Region (NCR). This is achieved through a nested configuration of domains in the WRF model as shown in Figure 1a, utilizing the reference latitude of 28.6º N and longitude of 77.219º E as the center for coarser Domain-1 (D1). Encompassing an extensive area of 2,200,000 km^2, D1 spans northern India, parts of Pakistan and Afghanistan to the west, and the western reaches of China. Domain-2 (D2) covers a more confined area of 36,481 km^2, including the Delhi region and major neighboring cities such as Gurugram, Faridabad, Ghaziabad, Greater Noida, as well as smaller urban centers like Rohtak, Sonipat, Panipat, Meerut, and Muzaffarnagar to the north. The terrain height in the Delhi urban region varies from 210 to 220 m above mean sea level (AMSL). The nested domains have a grid spacing ratio of 1:5, with different grid resolutions for each domain. D1 has a grid spacing of 5 km, while D2 has a finer resolution with a grid spacing of 1 km. The grid configurations for D1 and D2 are 440 x 200 and 191 x 191, respectively. To capture the vertical structure of the atmosphere, the model employs 54 vertical eta levels, extending up to the 50 hPa pressure height. The first seven layers are within a height of 30 meters above ground level (AGL), followed by around ten layers within 60 meters AGL, and 19 layers extending up to 1 km AGL to effectively capture the boundary layer processes. Additional details regarding the

various physics options and model configuration settings used in the study are provided in Table 1.

The default United States Geological Survey (USGS)-24 category, which was created in WRF V3.8 based on the 1992-93 Global Land Cover Characterization (GLCC) data at a resolution of 30 arc-seconds, has become obsolete and inadequate for accurately representing urban classification within and around urban regions like Delhi. Therefore, in the present study, the land use land cover (LULC) has been updated entirely over the Delhi region (Figure 1b) using the recently released (October 28, 2022) European Space Agency (ESA) World-Cover 2021 data (https://worldcover2021.esa.int). This dataset boasts a higher resolution of 10 m. The updated dataset is derived from data furnished by Sentinel-1 (Synthetic Aperture Radar) and Sentinel-2 (High-Resolution Optical Earth Observation Data) satellites. It was made public on October 28, 2022, and demonstrates an overall global accuracy of 76.7% (Van De Kerchove et al., 2021). The updated LULC, obtained by resampling the ESA data at a resolution of 30 arc-sec (~1 km), exhibits good agreement with the actual urban distribution observed in satellite images. This agreement extends to other categories present in the region covered by D2 (Figure 1c). The elevation in domain D2 is approximately 300 m AMSL, with irrigated cropland being dominant in the northeast. The remaining area encompasses dryland, shrubland, and water bodies.

2.2 Urban Morphological Parameters Datasets

To implement the coupled WRF-UACM model over Delhi region, urban morphological parameters have been considered. These parameters include average building height (H), plan area density (λ_p), frontal area density (λ_f), and street canyon orientation (φ). These parameters have been meticulously developed for the Delhi region (shown in Figure 2), attributed to each 1 km^2 urban grid cell in D2, utilizing the methodology described in Bhautmage et al. (2022). In deriving the first three parameters, the building polygon shapefile of the UT-GLOBUS dataset (Kamath et al., 2022) has been employed in conjunction with embedded building height data pertinent to the Delhi region. Evidently, the H ranges from ~8 to 10 m across the region, escalating to 12 to 14 m within densely populated sectors. On the outskirts of the city, λ_p is ~0.1, and in the inner regions it is ~0.4 with some areas reaching a maximum density of 0.8 in extremely dense regions. Within the inner city, λ_f varies from 0.4 to 0.6, surpassing 1.0 in regions marked by extensive urbanization. The urban grid cells in D2 for which there are no

urban morphological parameters data available, default values of 6 m, 0.45, and 0.45 have been assumed for H, λ_p, and λ_f, respectively.

From these parameters data, the generalized information of street canyon width (W) and building width (B) can be obtained to ingest the urban geometry in a repeating canyon form into the model. Additionally, the requisite values of other parameters like sky view factors for road (ψ_r) and walls (ψ_w) for each urban grid cell, are also estimated based on the canyon dimensions (H, W) following the methodology in Masson (2000). The street canyon orientation parameter (φ) data, which represents the dominant street angle at which the majority of streets are aligned, is obtained for each urban grid cell by processing the street-map shapefile of the Delhi region (Geofabrik, 2018) obtained from https://www.geofabrik.de/data/download.html in the Geographic Information System (GIS) software. Employing a length weighting approach, emphasis is accorded to longer street canyon lengths. Predominantly, the canyon orientation within Delhi city adheres to the north-south direction, while less densely populated outskirts exhibit an east-west orientation.

2.3 Observational Sites and Datasets

To evaluate the performance of the WRF-UACM over the Delhi region, meteorological observations from ground-based stations are used. These stations (depicted in Figure 1d) are strategically positioned in urban areas, covering areas with low, mid, and high urban development. Specifically, the Delhi University, Akshardham, and Pitampura stations reside within densely populated urban regions, while Narela, Mungeshpur, Jafarpur, and Ayanagar stations are situated on the outskirts of Delhi, encompassing less densely populated areas. Frequent fog episodes having wide-spread nature occur during the winter season in the IGP region, often resulting in reduced visibility below 1 km and sometimes few tens of meters (very dense fog events). Consequently, to gain insights into the fog genesis, lifecycle, and mechanisms behind the spatiotemporal variations, the Winter Fog Experiment (WiFEX; Ghude et al., 2017) field campaigns have been conducted at the Indira Gandhi International Airport (IGIA) site (28.56 ºN, 77.09 ºE, 216 m AMSL) in New Delhi. The WiFEX campaigns have taken place during the winter season (December-February) since 2015 (Ghude et al., 2023, 2017). For the present study, observation data from the 2017-18 WiFEX campaign at the IGIA site were also utilized to evaluate the model performance.

The observation data used for model verification include measurements of relative humidity (RH) and air temperature (T) measured at a height of 2-meters. These measurements were obtained using a T and RH sensor (HMP45C Vaisala Oyj, Finland) installed on a 20-meter tower, with a temporal sampling frequency of 1-minute. Wind Speed (WS) data at a height of 10-meter were obtained using multicomponent weather sensors (WXT 520, Vaisala Oyj, Finland) installed on the same 20-meter tower with a temporal sampling frequency of 1-minute. Additionally, apart from the IGIA site data, meteorological data from other stations, including the radiosonde profile data at Ayanagar (which provides vertical profiles of wind speed, temperature, and humidity), were obtained from the Indian Meteorological Department (IMD, Delhi). All meteorological data collected at a higher temporal sampling frequency of 1-minute were subsequently aggregated over hourly periods for model verification purposes.

2.4 Case Studies and Model Simulation Details

Two cases have been identified to evaluate the performance of the model. The first case pertains to a dense radiation fog event that occurred on January 29-30, 2017. Throughout this period, the prevailing wind direction over the IGP region was predominantly westerly and north-westerly. Prior to the onset of the fog at IGIA, the wind conditions were calm (wind speed less than 2 m s^{-1}), indicating minimal wind movements. The onset of fog was at 00:00 local time (IST-Indian Standard Time) on January 30th (18:30 UTC on 29 January) and dissipated completely by the morning of the same day at 11:00 IST, thus sustaining the fog for a total of 11 hours. The fog was determined by a visibility threshold of 1000 meters. Notably, during this event, the visibility at the IGIA site reached its lowest point, dropping to around 92 meters at 05:00 IST on January 30th, 2017. This case has been selected to evaluate the model's performance in accurately capturing the characteristics and dynamics of the radiation fog event, including visibility conditions.

The second case selected for assessing the UACM model performance involves clear sky conditions (no-fog case) from December 20-22, 2016. During this period, the prevailing winds also originated from the west and northwest, however, the wind speeds were higher (> 2.0 m s^{-1}) compared to the fog episode. Analysis of the WiFEX (2015-16) campaign (Ghude et al., 2017) data revealed that the RH remained below 80%, cloud cover was less than 25%, and visibility consistently exceeded 2000 meters throughout the entire period. This case has been selected to

examine the model's ability to accurately reproduce meteorological conditions in scenarios characterized by clear skies, the absence of clouds and rainfall, and the presence of abundant sunshine.

For both the selected cases, the model simulations were conducted by performing a model spin-up process for both the baseline WRF-BACM (WRF-Base Asymmetric Convective Model, WRF V3.8 model control runs with the default existing base PX-LSM and base ACM2-PBL scheme, and without using any other existing explicit urban modeling option and urban morphological parameters dataset) and WRF-UACM. The fog-event model-run was initialized on January 29, 2017, at 00:00 UTC, with a 6-hour spin-up time to ensure the model reached a stable state at least 18 hours before the onset of fog. Similarly, the clear sky case was initialized on December 19, 2016, at 00:00 UTC, with a same spin-up period to establish model stability before the actual simulation analysis time began.

Typically, when simulations are conducted for regional weather forecasting using the WRF model, the minimum required input data includes the initial and boundary meteorological conditions for all nested domains, as well as land-use category data specifying fractions for urban, vegetation, and other categories. Additional useful data encompassed detailed soil and vegetation classification categories, along with their corresponding thermal and hydraulic properties. The initial and boundary meteorological conditions for the simulations are acquired from the National Centers for Environmental Prediction (NCEP) final analysis (FNL) data. This dataset is produced by conducting global forecast system simulations using observations from around the globe. The selected NCEP data has a spatial resolution of 1^{o} in both latitude and longitude, and a temporal resolution of 6 hours. The updated USGS-Sentinel land use data is utilized for both WRF-BACM and WRF-UACM simulations. However, the WRF-UACM runs require additional urban morphological parameters such as average building height (H), plan area density (λ_p), frontal area density (λ_f), and street canyon orientation (φ).

3. Results and Discussion

In this section, the UACM's performance is meticulously assessed across both case studies discussed in Section 2.4, offering a comprehensive presentation of detailed comparisons and result analysis together with the BACM model. A profound understanding of the simulations for each case emerges through spatial plots showcasing model discrepancies between the UACM

and BACM across T2, RH2, LWC and WS10. Furthermore, spatial plots of UACM-simulated surface LWC during the fog dissipation hours are presented, along with a comparison to NASA's MODIS satellite image taken around 10:30 am IST. These comparisons highlight the UACM's ability to capture fog dynamics and the burn-off mechanism during the dissipation over the urbanized Delhi region. Time-series analysis of the bias (Model – Observation) for T2, RH2 and WS10 is conducted at various meteorological stations in the urban region of Delhi-NCR. Additionally, comparison of modeled results for the vertical profiles of RH, potential temperature (θ), and WS were made using the radiosonde data collected at the Ayanagar station. Overall, this analysis provides insights into the performance of the UACM and its skill in simulating urban fog characteristics. Similarly, the UACM's competence in replicating meteorological conditions during clear sky events is also analyzed. The focus of this assessment is to evaluate how accurately the UACM represents crucial meteorological variables such as temperature, humidity, and wind speed during periods characterized by clear sky conditions.

3.1 Fog Case (January 29-30, 2017)

Figures 3(a-d), 3(e-h), 3(i-j), and 3(m-p) present the model differences between UACM and BACM for near surface T2, RH2, LWC, and WS10 variables, respectively, at key timings: 21:00 IST (15:30 UTC, 29-Jan), 03:00 IST (21:30 UTC, 29-Jan), 06:00 IST (00:30 UTC, 30-Jan), and 09:00 IST (03:30 UTC, 30-Jan). These time intervals correspond to the stages before, during, mature, and the posterior fog conditions. The BACM model simulates much lower urban temperatures compared to UACM caused by a rapid drop in temperature after sunset over the Delhi-NCR region as shown in Figure 3a. The absence of the UHI effect in the BACM leads to a rapid cooling in nocturnal temperatures, which further contributes to the steep increase in RH2 and LWC. Moreover, the adjacent regions surrounding the city area also display enhanced levels of LWC in the BACM simulation (Figure 3i and 3j). This shift in LWC patterns from actual observations can be ascribed to their marginally lower temperatures and the windy conditions, including the influence of rural-urban breezes. These breezes facilitate the augmented influx of moisture from nearby sources such as irrigated croplands and the Yamuna River that flows through the city.

The UACM, on the other hand, proficiently captures the nocturnal UHI effect, demonstrating its efficacy in simulating temperature variations and urban climate characteristics

in comparison to the BACM. The UACM manifests higher T2 at 21:00 IST on 29 January and 03:00 IST on 30 January (Figure S3 in the supporting information). This higher temperature is attributed to the release of daytime stored heat in the urban infrastructure back into the atmosphere and limited sky-view from the street which reduces radiative cooling. The impact of UACM on LWC is particularly evident over urban areas during the nighttime fog period as shown in Figures 3(i-k). This decrease in LWC is most pronounced before the onset of fog at 21:00 IST, revealing the UACM's ability to effectively reduce LWC.

The reduction in the magnitudes of wind speed by 0.5-2.0 m s^{-1} over the urban region in the UACM compared to the BACM as shown in Figures 3(m-p) is mainly attributed to the momentum drag resulting from the explicit inclusion of urban structures in the model. Urban morphological parameters like building heights, frontal area, and street orientation significantly contribute to the reduction in wind speed within urban domains (More details can be found in Figures S1, S2, and S5 in the supporting information).

In Figures 4(a-b), spatial plots illustrate the UACM-simulated near-surface LWC at 10:00 IST and 11:00 IST, while Figure 4c presents NASA's MODIS sensor-captured satellite image around ~10:30 IST in the morning. The MODIS image clearly depicts the burn-off (dissipation) of fog layers over the urban areas including Delhi, forming a clear area or "hole" within the city, while the fog persists in the surrounding areas. The UACM simulation shows low LWC values over the urbanized areas at both 10:00 IST and 11:00 IST, aligning well with the spatial pattern observed in the MODIS satellite image. This agreement between the UACM simulation and the satellite image indicates the model's ability to capture the fog burn-off process and the influence of urban heat release on dissipating fog over urban areas.

Figures 5(a-c) present time-series plots depicting the bias between modeled data and observations for T2, RH2, and WS10, respectively, at six stations in Delhi-NCR. The bold lines in the plots represent the bias of UACM values compared to the observations, while the dashed lines indicate the bias exhibited by the BACM. Positive values indicate over-prediction, whereas negative values indicate under-prediction. Notably, the UACM excels during the fog period (from 29-Jan-2017, 23:00 IST to 30-Jan-2017, 11:00 IST), closely aligning with observed conditions. The UACM reduced overestimation of daytime T2 compared to BACM by generating a cooling effect due to the combined influence of urban structures and the solar zenith angle. The model also released daytime stored heat during nighttime hours, resulting in warmer

temperatures compared to the BACM. Particularly noteworthy is the UACM accurately simulating the nighttime UHI effect. The diurnal trend of RH2 is also effectively captured by the UACM as seen in Figure 5b, thus reducing bias. While UACM slightly underestimates RH2 before the night of fog onset, it demonstrates improvement the following day post-event. Lastly, the UACM significantly improved the prediction of WS10 at Delhi stations, closely aligning with observed data (Figure 5c). This reduction in bias indicates the UACM's ability to simulate wind patterns within the urban canopy. During fog episodes, the UACM adeptly reproduces calm wind conditions, effectively modeling meteorological aspects of fog events, such as low wind speeds under stable atmospheric conditions. Overall, the UACM proficiently reproduces fog event meteorology, leading to improved predictions for T2, RH2, and WS10 compared to the BACM.

Figure 5d illustrates the time-series comparison of LWC predicted by BACM and UACM models, alongside observed horizontal visibility at IGIA. UACM consistently simulates lower LWC values (0-0.4 g m^{-3}) due to liquid droplet evaporation from higher temperatures and air remaining away from saturation point in urban regions. The UACM demonstrates a significant improvement in fog forecasting compared to the BACM, as evidenced from improvement in the fog onset time prediction by a delay of approximately 3 hours in the predicted LWC values. The onset of fog, indicated by visibility dropping below 1000 m (moderate fog conditions), aligns well with the UACM's delayed LWC prediction. As the LWC values rise and reach their peak, visibility starts dropping below 500 m, indicating the presence of dense fog. During the period of dense fog (04:00 IST - 09:00 IST, 30 January), the UACM simulates LWC values ranging from 0.1 to 0.3 g m^{-3} with visibility declining to around 92 m at 05:00 IST on 30 January. In addition, the UACM demonstrates an early dissipation of fog compared to the BACM, resulting in the formation of clear areas or "holes" over urban regions due to the burned-off mechanism. During the dissipation phase of the fog after sunrise, the solar radiation reaching the ground surface intensifies in the morning hours and the surface temperature as well as the temperature in the boundary layer starts to rise. This triggers instability leading to an augmentation of vertical turbulent mixing and a concurrent reduction in RH near the surface. This phenomenon aligns well with the gradual increase in visibility observed at the IGIA site after sunrise (Figure 5d). When considering fog occurrences, the temporal variation of LWC from the WRF-UACM model closely matches the LWC profiles derived from microwave radiometer (MWR) observations

(visibility dropping below 500 m) at IGIA (Figurer 5e). It is noteworthy, that the model-derived LWC in Pithani et al., (2020) consistently exhibit an overestimation of LWC values when compared to the actual observations, thus falling short in accurately representing the true fog intensity. The implementation of the WRF-UACM led to a reduction in the overestimation of LWC values as observed in this study. The UACM's simulation of fog dissipation and the corresponding improvement in visibility corroborate its ability to capture the dynamic nature of fog events in the study area.

During a fog episode, the UACM performance is better than BACM, particularly for the WS10, T2, and RH2 with index of agreement (IOA) of 0.89, 0.96, and 0.92, respectively. Mean bias (MB) and Mean error (ME) are reduced to 0.14 and 0.36 m s^{-1} by the UACM for WS10 (i.e., 73.07% and 47.8% improvement, respectively). Similarly, normalized mean bias (NMB) is reduced by 29% and normalized mean error (NME) by 24% for WS10. The root mean squared error (RMSE) for BACM of 0.9 m s^{-1} is improved to 0.46 m s^{-1} with the UACM. The under-prediction in T2 (MB and NMB) is greatly reduced by the UACM compared to BACM. Also, the T2 ME and NME decreased in the UACM by 0.83 °C and 6% relative to the BACM. The metrics for RH2 other than IOA have shown a slight decrease in the performance by the UACM. A comparison of different statistical metrics for T2, RH2 and WS10 using the BACM and UACM models can be found in Table 2 while the definitions of the statistical metrics can be found in Appendix A.

Figures 6(a-c) show vertical profiles of the RH, potential temperature (θ), and WS at the Ayanagar station during the dense fog event on 30-Jan-2017 at 05:30 IST. These profiles offer valuable insights into the atmospheric stability conditions during the fog event. As depicted in Figure 6a, the RH profile illustrates that there is a complete air saturation (RH = 100%) within the depth of the fog layer. The UACM simulated a fog layer thickness of up to 60 meters, which was 30 meters lower than the BACM. The higher temperatures over the urban region due to the UHI effect, resulted in less condensation of liquid droplets in the UACM and a lower fog layer depth. It is worth noting that the observation profile exhibited an even smaller depth of fog layer. This difference could be due to the 1-km horizontal grid spacing of the model and a possible interpolation error while using the nearest model grid cell for comparison. Figure 6b presents the vertical profile for θ. Both models show a well-mixed layer condition within the fog layer depth, indicating neutral stability. However, there is a slight instability near the ground due to the

warmer temperatures near the surface caused by the UHI effect, longwave warming inside the fog layer, and latent heat released during the liquid condensation process. In Figure 6c, the wind speed profiles demonstrate that the wind does not follow a logarithmic pattern within the urban canopy layer. Instead, the wind gradually decreases due to calm wind conditions and the influence of the urban environment within the fog layer depth. Above the fog layer, the wind profiles exhibit a logarithmic pattern, indicating a more stable atmospheric layer. Overall, the vertical profiles provide valuable information about the atmospheric stability conditions during the dense fog event and highlight the impact of the UHI effect on fog layer depth, the well-mixed layer condition within the fog layer, and the gradual decrease in wind speed within the urban canopy.

3.2 Clear Sky Case (December 20-22, 2016)

Figures 7(a-d) illustrate spatial T2 differences (UACM – BACM) at 06:00 IST, 09:00 IST, 21:00 IST, and 03:00 IST on 20-Dec-2016 with clear skies and abundant sunshine (no-fog case). The UACM is considerably warmer than BACM at night (06:00 IST, 21:00 IST, and 03:00 IST) but similar (09:00 IST, Figure 7b) or slightly cooler (14:00 IST, Figure S7b in the supporting information) during daytime. UACM reveals 8-18% RH2 reduction over urban areas compared to BACM (Figures 7(e-h)), which stems from nighttime urban warming, thereby urban air remaining away from the saturation point as discussed in the previous section. The spatial difference in wind speeds using BACM and UACM models presented in Figures 7(i-l) showed reduced wind speeds in UACM simulations, owing to appropriate consideration of momentum drag due to the presence of buildings (Figure S8 in the supporting information). In contrast, the surrounding regions of the urban areas exhibit slight increases in wind speeds. This could be due to the formation of rural-urban breezes, which are influenced by temperature variations and pressure gradients that drive the movement of air, between urban and rural areas, resulting in slightly windy conditions in the surrounding areas compared to the urban core.

Figures 8(a-c) depict the time-series plots of the bias between the modeled data and observations for T2, RH2, and WS10. Bold and dashed lines represent the bias of UACM and BACM, respectively. Positive values denote over-prediction; negative values signify under-prediction. Closer trends to zero-line suggest reduced differences. The UACM demonstrates significant enhancements in simulating daytime T2, as illustrated in Figure 8a. The model

successfully reduced the bias by creating a cooling effect during daytime, which mitigates the over-prediction of daytime temperatures exhibited by the BACM. The UACM has also reduced the daytime RH2 bias in Delhi, as depicted in Figure 8b. However, during nighttime, the UACM exhibits a dry bias compared to the BACM. This is due to the over-prediction of nighttime temperatures (warm bias) by the UACM possibly due to increased absorption of daytime sun rays and their multiple reflections within the canyons, which leads to the excessive evaporation and consequently lower moisture content. Nevertheless, certain stations such as Ayanagar, Jafarpur, and Akshardham demonstrate improvements in simulating nighttime temperatures. The UACM demonstrates improvements in simulating WS10 by accounting for the influence of urban structures and their effects on wind flow, as evident from the time-series plots at all the meteorological stations considered (Figure 8c). The statistical analysis presented in Table 2 shows that the overall performance of UACM is better compared to BACM under clear sky conditions.

Figure 6 (d-f) presents the vertical profiles of RH, potential temperature (θ), and WS simulated by the UACM and BACM, along with the comparison to radiosonde observations at Ayanagar station. The RH profiles exhibit a dry bias (under-prediction) compared to the observation profile. This under-prediction is mainly attributed to the higher temperatures simulated by the UACM near the urban ground surface and within the urban canopy, as shown in Figure 6d. Note that the UACM RH profile is almost a mirror image of the θ profile (Figure 6e). However, 90 meters AGL, the RH profiles for both models closely resemble each other. The potential temperature (θ) profiles demonstrate better agreement with the observation profile, particularly near the ground surface. The profiles exhibit a slightly convective nature at the Ayanagar station. Within the urban canopy, the UACM profiles show characteristics of a more well mixed layer up to a height of 50 m AGL, transitioning to a stable condition above it at 05:30 IST, as depicted in Figure 6e. The WS profiles exhibit a logarithmic nature within the urban canopy at Ayanagar station. The wind magnitude near the ground surface is approximately 3.0 m s^{-1} in the UACM, slightly deviating from the observed value. However, above the ground surface, some bias is still observed between the model profiles and the observation profile. This discrepancy may be attributed to the differences in distance between the nearby urban grid cell center and the exact location of the Ayanagar radiosonde observation site.

4. Summary

This study implemented the newly developed multilayer WRF-UACM by Dy et al. (2019) and Bhautmage et al. (2022) over the Delhi region for urban fog prediction application. The goal was to have an enhanced representation of the urban roughness sublayer and predict meteorological variables within the urban canopy layer using the WRF-UACM. We evaluated the model's capacity to forecast fog formation, by comparing with in-situ observations including those taken at the Indira Gandhi International Airport (IGIA) site in New Delhi during the Winter Fog Experiment (WiFEX; Ghude et al., 2017) field campaign. The implementation of WRF-UACM over the Delhi region showed noteworthy improvements in urban meteorology within the boundary layer, both during a clear-sky period and a foggy event. Predictions for parameters such as 10-meter wind speed (WS10), 2-meter temperature (T2), and 2-meter relative humidity (RH2) exhibited good agreement with observations from meteorological stations in Delhi. Notably, the UACM has contributed to the faster dissipation of fog compared to control (WRF-BACM) model runs, and this alignment with satellite images from NASA's MODIS sensor confirmed the clearing of fog over Delhi's urban region. In addition to the urban morphology, topography, and surface characteristics, the fog episodes are also influenced by numerous other factors such as synoptic scale weather patterns, regional moisture intrusion, aerosol loading, and microphysics related to the fog formation etc. The UACM model also demonstrated advancements in simulating fog timing, onset, and dissipation compared to visibility and liquid water content (LWC) observations at the IGIA site. Due to its computational efficiency, UACM is well-suited for operational fog forecasting. This has significant benefits for transportation and aviation sectors, reducing economic losses, health risks, and potential accidents due to low visibility. Overall, implementing UACM in operational mode, especially during winter, presents substantial advantages, as this study demonstrates. Moreover, assessing its performance in predicting various fog types like advection-radiation, cloud-base-lowering, evaporation, and precipitation fog would enhance the model's robustness. By offering improved accuracy in simulating urban meteorology and forecasting fog events, the model facilitates timely preventive actions and mitigates potential disruptions across sectors.

Acknowledgements

We are thankful to Dr. Narendra Nigam from the Indian Meteorological Department (IMD), New Delhi, India for providing the essential meteorological stations data in the urbanized region of Delhi. Special thanks are also to the High-Performance Computing (HPC) Pratyush team at the Indian Institute of Tropical Meteorology (IITM), Pune, India for their continuous technical support in assisting with the WRF-UACM model setup and compiling issues. The authors also acknowledge GMR and Airport Authority of India for their logistic support at IGI Airport New Delhi. Finally, we would like to thank reviewers for their insightful and invaluable comments for improving the manuscript.

Appendix A: Statistical Metrics Definitions

In this study, the performance of the models is assessed using several statistical parameters, including the index of agreement (IOA), root mean square error (RMSE), mean bias (MB), normalized mean bias (NMB), mean error (ME), and normalized mean error (NME). The IOA measures the agreement between the model predictions and observations, with a value of 1 indicating a perfect match and 0 indicating no agreement (Willmott, 1981). The RMSE and ME provide information about the average error in absolute magnitudes. The NME, expressed as a percentage, represents the average error relative to the observed values, where a higher NME indicates a greater error, and a lower value indicates a lesser error in the predictions. The MB indicates whether the model overestimates or underestimates compared to the observations. The NMB, also expressed as a percentage, indicates the average bias relative to the observed values, with a positive NMB indicating overestimation and a negative NMB indicating underestimation of the magnitudes. N is the total number of observations over a period at each individual meteorological station; M_i is the ith model simulated value corresponding to the ith observation value O_i; $\underline{O}$ is the average of observation values over a period.

$$IOA = 1 - \frac{\sum_{i=1}^{N}(M_i - O_i)^2}{\sum_{i=1}^{N}(|M_i - \underline{O}| + |O_i - \underline{O}|)^2} \qquad \text{(Eqn. A1)}$$

$$RMSE = \left[\frac{1}{N}\sum_{i=1}^{N}(M_i - O_i)^2\right]^{\frac{1}{2}} \qquad \text{(Eqn. A2)}$$

$$MB = \frac{\sum_{i=1}^{N}(M_i - O_i)}{N} \quad \text{(Eqn. A3)}$$

$$NMB = \frac{\sum_{i=1}^{N}(M_i - O_i)}{\sum_{i=1}^{N} O_i} \quad \text{(Eqn. A4)}$$

$$ME = \frac{\sum_{i=1}^{N}|M_i - O_i|}{N} \quad \text{(Eqn. A5)}$$

$$NME = \frac{\sum_{i=1}^{N}|M_i - O_i|}{\sum_{i=1}^{N} O_i} \quad \text{(Eqn. A6)}$$

Disclaimer:

Although this work was reviewed by the United States Environmental Protection Agency (USEPA) and approved for publication, it may not necessarily reflect official Agency policy. The mention of commercial products does not constitute endorsement by the Agency.

Data Availability Statement

Meteorological station observation data provided by the Indian Meteorological Department (IMD, Delhi) https://rmcnewdelhi.imd.gov.in and Winter Fog Experiment (WiFEX 2017-18 Field Campaign) have been used to compare the models' performance in this manuscript. The WiFEX field campaign data at Indira Gandhi International Airport (IGIA), New Delhi, India is available from https://ews.tropmet.res.in/wifex/observations.php [Dataset].

The urban land-use data have been updated in the Delhi region from the European Space Agency (ESA) World Cover 2021 data (released on October 28, 2022) based on Sentinel-1 and Sentinel-2 satellite data which is available at https://worldcover2021.esa.int [Dataset].

The urban morphological parameters dataset required to run the WRF-UACM model were developed by using the Geographic Information System (GIS) (ArcGIS V10.5.1) software, which can be accessed at https://www.esri.com/en-us/arcgis/products/arcgis-pro/overview [Software].

The Delhi region building shapefile along with the embedded building height data has been used to derive the urban morphological parameters which has been obtained from the UT-GLOBUS dataset (Kamath et al., 2022) [Dataset].

OpenStreetMap shapefile obtained from https://www.geofabrik.de/data/download.html has been used to develop street orientation parameter in the GIS (ArcGIS V10.5.1) software [Dataset].

The state-of-the-art Weather Research and Forecasting (WRF V3.8) model is available at https://www2.mmm.ucar.edu [Software]. The meteorological input data to create the initial and boundary conditions for the WRF model domains were obtained from the National Centers for Environmental Prediction (NCEP) FNL (Final) Operational Global Analysis data available at https://rda.ucar.edu/datasets [Dataset].

Figures have been made with the National Center for Atmospheric Research (NCAR) Command Language (NCL V6.3.0) post-processing tool accessible at https://www.ncl.ucar.edu [Software] and wrf-python plotting package available at https://anaconda.org/conda-forge/wrf-python [Software]. The radiometer liquid water content plot has been prepared with RPG-HATPRO Humidity and Temperature Profiler V8.79 [Software].

Radiosonde profiles at IMD, Ayanagar Station, New Delhi, India during study period are available from the Wyoming website: https://weather.uwyo.edu/upperair/sounding.html.
LWC Plot was created using RAOB V6.8 [Software].

References

AMS Glossary. (2020). *American Meteorological Society*. https://glossary.ametsoc.org/wiki/Urban_heat_island.

Bari, D., Bergot, T., & Tardif, R. (2023). Fog Decision Support Systems: A Review of the Current Perspectives. *Atmosphere, 14*(8), 1314. https://doi.org/10.3390/atmos14081314.

Bergot, T., and D. Guedalia (1994). Numerical forecasting of radiation fog. Part I: Numerical model and sensitivity tests. *Mon. Wea. Rev.*, 122 , 1218–1230. https://doi.org/10.1175/1520-0493(1994)122<1218:NFORFP>2.0.CO;2.

Bergot, T., Escobar, J., & Masson, V. (2015). Effect of small-scale surface heterogeneities and buildings on radiation fog: Large-eddy simulation study at Paris–Charles de Gaulle airport. *Quarterly Journal of the Royal Meteorological Society, 141*(686), 285-298. https://doi.org/10.1002/qj.2358

Bhautmage, U. P., Fung, J. C. H., Pleim, J., & Wong, M. M. F. (2022). Development and Evaluation of a New Urban Parameterization in the Weather Research and Forecasting (WRF) Model. *Journal of*

Geophysical Research: Atmospheres, *127*(16), e2021JD036338. https://doi.org/10.1029/2021JD036338.

Bhowmik, S. R., Sud, A. M., & Singh, C. (2004). Forecasting fog over Delhi-An objective method. *Mausam*, *55*(2), 313-322. https://doi.org/10.54302/mausam.v55i2.1096

Bhushan, B., Trivedi, H. K. N., Bhatia, R. C., Dube, R. K., Giri, R. K., & Negi, R. S. (2003). On the persistence of fog over northern parts of India. *Mausam*, *54*(4), 851-860.

Bougeault, P., & Lacarrere, P. (1989). Parameterization of orography-induced turbulence in a mesobeta-scale model. *Monthly Weather Review*,*117*(8), 1872–1890. https://doi.org/10.1175/1520-0493(1989)117<1872:pooiti>2.0.co;2

Chen, F., & Dudhia, J. (2001). Coupling an advanced land surface–hydrology model with the Penn State-NCAR MM5 modeling system. Part I: Modelimplementation and sensitivity. *Monthly Weather Review*, *129*(4), 569–585. https://doi.org/10.1175/15200493(2001)129<0569:caalsh>2.0.co;2

Chen, F., Kusaka, H., Bornstein, R., Ching, J., Grimmond, C. S. B., Grossman-Clarke, S., et al. (2011). The integrated WRF/urban modelling system: Development, evaluation, and applications to urban environmental problems. *International Journal of Climatology*, *31*(2), 273–288. https://doi.org/10.1002/joc.2158

Dhangar, N. G., Lal, D. M., Ghude, S. D., Kulkarni, R., Parde, A. N., Pithani, P., ... & Rajeevan, M. (2021). On the conditions for onset and development of fog over New Delhi: an observational study from the WiFEX. *Pure and Applied Geophysics*, *178*, 3727-3746. https://doi.org/10.1007/s00024-021-02800-4

Dhangar, N. G., and Coauthors (2022). Fog nowcasting over the IGI Airport, New Delhi, India using decision tree. *Mausam*, **73**, 785–794, https://doi.org/10.54302/mausam.v73i4.3441.

Dy, C. Y., Fung, J. C. H., & Pleim, J. (2019). Momentum drag effect over urbanized areas in the ACM2 PBL component of the WRF model. *Journal of Geophysical Research: Atmospheres*, *124*(8), 4460-4476. https://doi.org/10.1029/2018JD029333

Gao, X., Gao, S., & Yang, Y. (2018). A comparison between 3DVAR and EnKF for data assimilation effects on the Yellow Sea fog forecast. *Atmosphere*, *9*(9), 346. https://doi.org/10.3390/atmos9090346

Gautam, R., Hsu, N. C., Kafatos, M., & Tsay, S. C. (2007). Influences of winter haze on fog/low cloud over the Indo-Gangetic plains. *Journal of Geophysical Research: Atmospheres*, *112*(D5). https://doi.org/10.1029/2005JD007036

Gautam, R., & Singh, M. K. (2018). Urban heat island over Delhi punches holes in widespread fog in the Indo-Gangetic Plains. *Geophysical Research Letters*, *45*(2), 1114-1121. https://doi.org/10.1002/2017GL076794

Geofabrik Download Server. (2018). OpenStreetMap Data Extracts [WWW Document]. Retrieved from https://www.geofabrik.de/data/download.html

Ghude, S. D., Bhat, G. S., Prabhakaran, T., Jenamani, R. K., Chate, D. M., Safai, P. D., ... & Rajeevan, M. (2017). Winter fog experiment over the Indo-Gangetic plains of India. *Current Science*, 767-784. DOI:10.18520/cs/v112/i04/767-784.

Ghude, S. D., Jenamani, R. K., Kulkarni, R., Wagh, S., Dhangar, N. G., Parde, A. N., ... & Rajeevan, M. (2023). WiFEX: Walk into the Warm Fog over Indo-Gangetic Plain Region. *Bulletin of the American Meteorological Society*, *104*(5), E980-E1005. https://doi.org/10.1175/BAMS-D-21-0197.1

Gu, Y., Kusaka, H., & Tan, J. (2019). Impacts of urban expansion on fog types in Shanghai, China: Numerical experiments by WRF model. *Atmospheric Research*, *220*, 57-74. https://doi.org/10.1016/j.atmosres.2018.12.026

Gunturu, U. B., & Kumar, V. (2021). Weakened Baroclinic Activity Causes an Abrupt Rise in Fog in the Indo-Gangetic Plain. *Geophysical Research Letters*, *48*(24), e2021GL096114. https://doi.org/10.1029/2021GL096114

Hendricks, E. A., Knievel, J. C., & Wang, Y. (2020). Addition of multilayer urban canopy models to a nonlocal planetary boundary layer parameterization and evaluation using ideal and real cases. *Journal of Applied Meteorology and Climatology*, *59*(8), 1369-1392.

Hingmire, D., Vellore, R. K., Krishnan, R., Ashtikar, N. V., Singh, B. B., Sabade, S., & Madhura, R. K. (2019). Widespread fog over the Indo-Gangetic Plains and possible links to boreal winter teleconnections. *Climate Dynamics*, *52*, 5477-5506. https://doi.org/10.1007/s00382-018-4458-y

Hingmire, D., Vellore, R., Krishnan, R., Singh, M., Metya, A., Gokul, T., & Ayantika, D. C. (2021). Climate change response in wintertime widespread fog conditions over the Indo-Gangetic Plains. *Climate Dynamics*, 1-22. https://doi.org/10.1007/s00382-021-06030-1

Hong, S. Y., Noh, Y., & Dudhia, J. (2006). A new vertical diffusion package with an explicit treatment of entrainment processes. *Monthly Weather Review*, *134*, 2318–2341. https://doi.org/10.1175/MWR3199.1

Janjić, Z. I. (1994). The step-mountain eta coordinate model: Further developments of the convection, viscous sublayer, and turbulence closure schemes. *Monthly Weather Review*, *122*(5), 927–945. https://doi.org/10.1175/1520-0493(1994)122<0927:TSMECM>2.0.CO;2

Jayakumar, A., Rajagopal, E. N., Boutle, I. A., George, J. P., Mohandas, S., Webster, S., & Aditi, S. (2018). An operational fog prediction system for Delhi using the 330 m Unified Model. Atmospheric Science Letters, 19(1), e796. https://doi.org/10.1002/asl.796

Jayakumar, A., Gordon, H., Francis, T., Hill, A. A., Mohandas, S., Sandeepan, B. S., ... & Beig, G. (2021). Delhi Model with Chemistry and aerosol framework (DM-Chem) for high-resolution fog forecasting. *Quarterly Journal of the Royal Meteorological Society*, *147*(741), 3957-3978. https://doi.org/10.1002/qj.4163

Jenamani, R. K. (2007). Alarming rise in fog and pollution causing a fall in maximum temperature over Delhi. *Current Science*, 314-322. https://www.jstor.org/stable/24099461

Kamath, H. G., Singh, M., Magruder, L. A., Yang, Z. L., & Niyogi, D. (2022). GLOBUS: GLObal Building heights for Urban Studies. *arXiv preprint arXiv:2205.12224*

Kusaka, H., Kondo, H., Kikegawa, Y., & Kimura, F. (2001). A simple single-layer urban canopy model for atmospheric models: Comparison with multi-layer and slab models. *Boundary-Layer Meteorology*, *101*, 329–358. https://doi.org/10.1023/a:1019207923078

Müller, M. D., Schmutz, C., & Parlow, E. (2007). A one-dimensional ensemble forecast and assimilation system for fog prediction. *Pure and Applied Geophysics*, *164*, 1241-1264. https://doi.org/10.1007/s00024-007-0217-4

Martilli, A., Clappier, A., & Rotach, M. W. (2002). An urban surface exchange parameterisation for mesoscale models. *Boundary-Layer Meteorology*,*104*, 261–304. https://doi.org/10.1023/a:1016099921195

Masson, V. (2000). A physically-based scheme for the urban energy budget in atmospheric models. *Boundary-Layer Meteorology*, *94*, 357–397. https://doi.org/10.1023/a:1002463829265

Mellor, G. L., & Yamada, T. (1974). A hierarchy of turbulence closure models for planetary boundary layers. *Journal of the Atmospheric Sciences*, *31*(7), 1791–1806. https://doi.org/10.1175/1520-0469(1974)031<1791:ahotcm>2.0.co;2

Mellor, G. L., & Yamada, T. (1982). Development of a turbulence closure model for geophysical fluid problems. *Reviews of Geophysics*, *20*(4), 851–875. https://doi.org/10.1029/RG020i004p00851

Niu, G. Y., Yang, Z. L., Mitchell, K. E., Chen, F., Ek, M. B., Barlage, M., ... & Xia, Y. (2011). The community Noah land surface model with multiparameterization options (Noah-MP): 1. Model description and evaluation with local-scale measurements. *Journal of Geophysical Research: Atmospheres*, *116*(D12).

Pahlavan, R., Moradi, M., Tajbakhsh, S., Azadi, M., & Rahnama, M. (2021). Fog probabilistic forecasting using an ensemble prediction system at six airports in Iran for 10 fog events. *Meteorological applications*, *28*(6), e2033. https://doi.org/10.1002/met.2033

Parde, A.N., Ghude, S.D., Dhangar, N.G., Lonkar, P., Wagh, S., Govardhan, G., Biswas, M. and Jenamani, R.K. (2022a). Operational probabilistic fog prediction based on Ensemble Forecast System: A decision support system for fog. *Atmosphere*, *13*(10), 1608. https://doi.org/10.3390/atmos13101608.

Parde, A. N., Ghude, S. D., Sharma, A., Dhangar, N. G., Govardhan, G., Wagh, S., ... & Niyogi, D. (2022b). Improving simulation of the fog life cycle with high-resolution land data assimilation: A case study from WiFEX. *Atmospheric Research*, *278*, 106331. https://doi.org/10.1016/j.atmosres.2022.106331

Parde, A.N., Ghude S.D., Dhangar, N.G., Bhautmage, U.P., Wagh, S., Lonkar, P., Govardhan, G., Kumar, R., Biswas, M., Chen, F. (2023). Challenges in Simulating Prevailing Fog Types over Urban Region of Delhi, *under-review*.

Pithani, P., Ghude, S. D., Jenamani, R. K., Biswas, M., Naidu, C. V., Debnath, S., ... & Rajeevan, M. (2020). Real-time forecast of dense fog events over Delhi: The performance of the wrf model during the wifex field campaign. *Weather and Forecasting*, *35*(2), 739-756. https://doi.org/10.1175/WAF-D-19-0104.1

Price, J. D., A. Porson, and A. Lock (2015). An observational case study of persistent fog and comparison with an ensemble forecast model. *Bound.-Layer Meteor* ., 155, 301–327, https://doi.org/10.1007/s10546-014-9995-2.

Rémy, S., & Bergot, T. (2010). Ensemble Kalman filter data assimilation in a 1D numerical model used for fog forecasting. *Monthly weather review*, *138*(5), 1792-1810. https://doi.org/10.1175/2009MWR3110.1

Sachweh, M., & Koepke, P. (1997). Fog dynamics in an urbanized area. *Theoretical and Applied Climatology*, *58*, 87-93. https://doi.org/10.1007/BF00867435

Salamanca, F., & Martilli, A. (2010). A new building energy model coupled with an urban canopy parameterization for urban climate simulations—Part II. Validation with one dimension off-line simulations. *Theoretical and Applied Climatology*, *99*, 345–356. https://doi.org/10.1007/s00704-009-0143-8

Sawaisarje, G. K., Khare, P., Shirke, C. Y., Deepakumar, S., & Narkhede, N. M. (2014). Study of winter fog over Indian subcontinent: Climatological perspectives. *Mausam*, *65*(1), 19-28. https://doi.org/10.54302/mausam.v65i1.858

Singh, M.K., Gautam, R. (2022). Developing a long-term high-resolution winter fog climatology over south Asia using satellite observations from 2002 to 2020. *Remote Sens. Environ.* 279. https://doi.org/10.1016/j.rse.2022.113128

Singh, J. and Kant, S. (2006). Radiation fog over north India during winter from 1989-2004. *Mausam*, *57*(2), 271-290. https://doi.org/10.54302/mausam.v57i2.474

Singh, J., Giri, R. K., & Kant, S. (2007). Radiation fog viewed by INSAT–1 D and Kalpana Geo-Stationary satellite. *Mausam*, *58*(2), 251-260.

Skamarock, W. C., Klemp, J. B., Dudhia, J., Gill, D. O., Barker, D. M., Duda, M. G., ... & Powers, J. G. (2008). A description of the advanced research WRF Version 3, Mesoscale and Microscale Meteorology Division. *National Center for Atmospheric Research, Boulder, Colorado, USA*, *88*, 7-25.

Steeneveld, G.J., Ronda, R.J., Holtslag, A.A.M. (2015). The Challenge of Forecasting the Onset and Development of Radiation Fog Using Mesoscale Atmospheric Models. *Boundary-Layer Meteorol.* 154. https://doi.org/10.1007/s10546-014-9973-8

Theethai Jacob, A., Jayakumar, A., Gupta, K., Mohandas, S., Hendry, M. A., Smith, D. K., ... & Ghude, S. (2023). Implementation of the urban parameterization scheme in the Delhi model with an improved urban morphology. *Quarterly Journal of the Royal Meteorological Society*, *149*(750), 40-60. https://doi.org/10.1002/qj.4382

Van De Kerchove, R., Zanaga, D., Keersmaecker, W., Souverijns, N., Wevers, J., Brockmann, C., ... & Arino, O. (2021). ESA WorldCover: Global land cover mapping at 10 m resolution for 2020 based on Sentinel-1 and 2 data. In *AGU Fall Meeting Abstracts* (Vol. 2021, pp. GC45I-0915). https://worldcover2021.esa.int/

Wagh, S., Kulkarni, R., Lonkar, P. *et al.* (2023). Development of visibility equation based on fog microphysical observations and its verification using the WRF model. *Model. Earth Syst. Environ.* 9, 195–211 . https://doi.org/10.1007/s40808-022-01492-6

Willmott, C. J. (1981). On the validation of models. *Physical geography*, *2*(2), 184-194. https://doi.org/10.1080/02723646.1981.10642213

Yadav, P., Parde, A.N., Dhangar, N.G., Govardhan, G., Lal, D.M., Wagh, S., Prasad, D.S.V.V.D., Ahmed, R., Ghude, S.D. (2022). Understanding the genesis of a dense fog event over Delhi using observations and high-resolution model experiments. *Model. Earth Syst. Environ.* 8. https://doi.org/10.1007/s40808-022-01463-x

Zhou, B., & Du, J. (2010). Fog prediction from a multimodel mesoscale ensemble prediction system. *Weather and Forecasting*, *25*(1), 303-322. https://doi.org/10.1175/2009WAF2222289.1

Figures

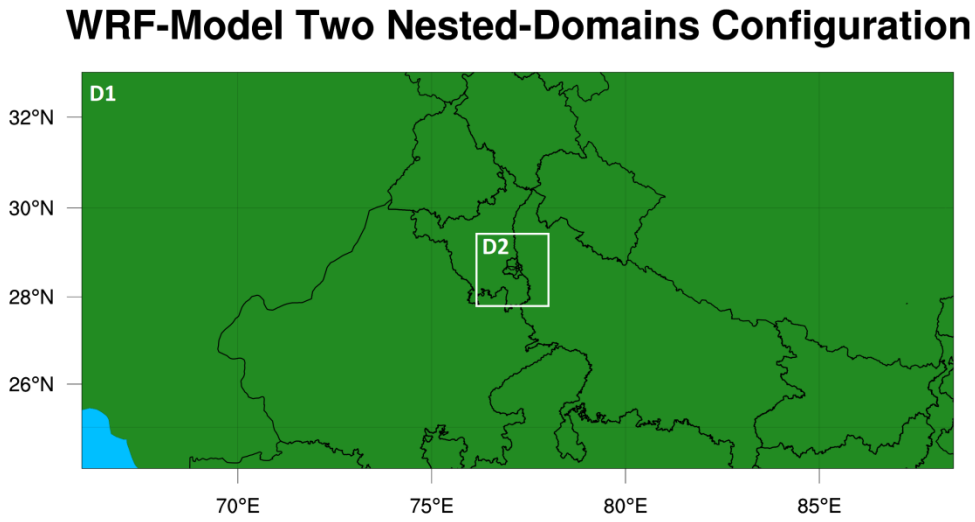

(a)

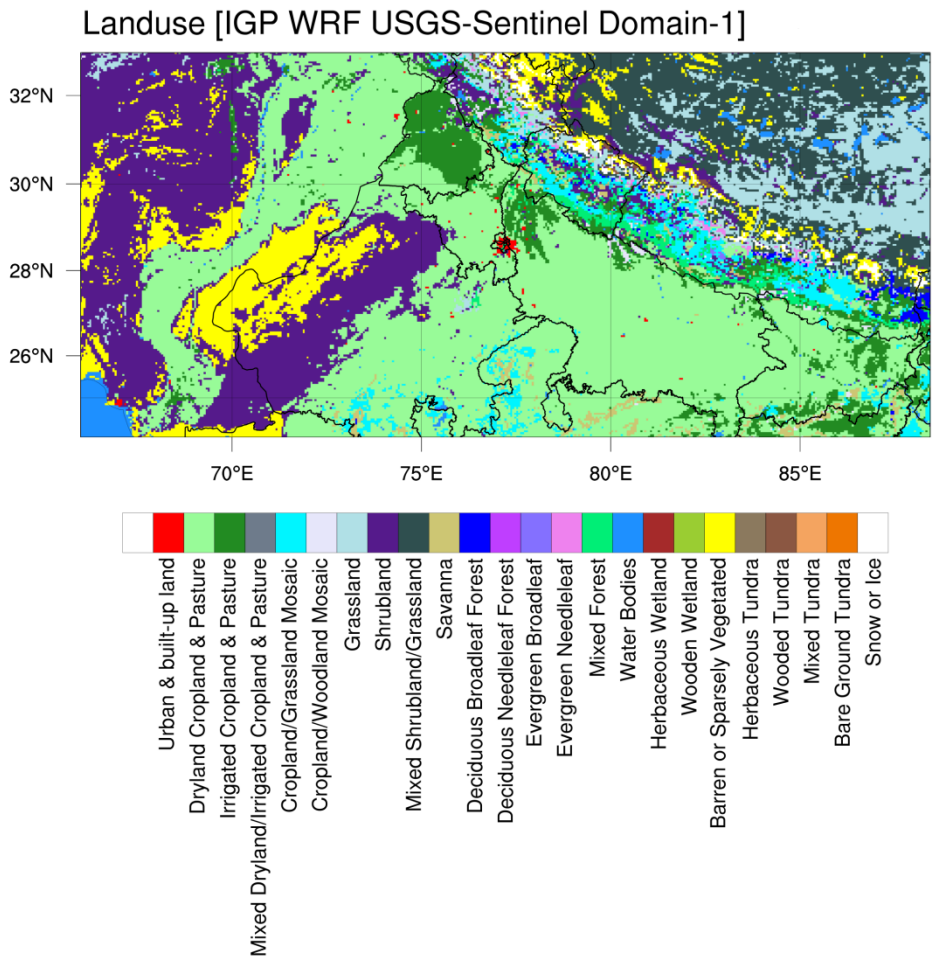
Landuse [IGP WRF USGS-Sentinel Domain-1]
32°N
30°N
28°N
26°N
70°E
75°E
80°E
85°E
Urban & built-up land
Dryland Cropland & Pasture
Irrigated Cropland & Pasture
Mixed Dryland/Irrigated Cropland & Pasture
Cropland/Grassland Mosaic
Cropland/Woodland Mosaic
Grassland
Shrubland
Mixed Shrubland/Grassland
Savanna
Deciduous Broadleaf Forest
Deciduous Needleleaf Forest
Evergreen Broadleaf
Evergreen Needleleaf
Mixed Forest
Water Bodies
Herbaceous Wetland
Wooden Wetland
Barren or Sparsely Vegetated
Herbaceous Tundra
Wooded Tundra
Mixed Tundra
Bare Ground Tundra
Snow or Ice

(b)

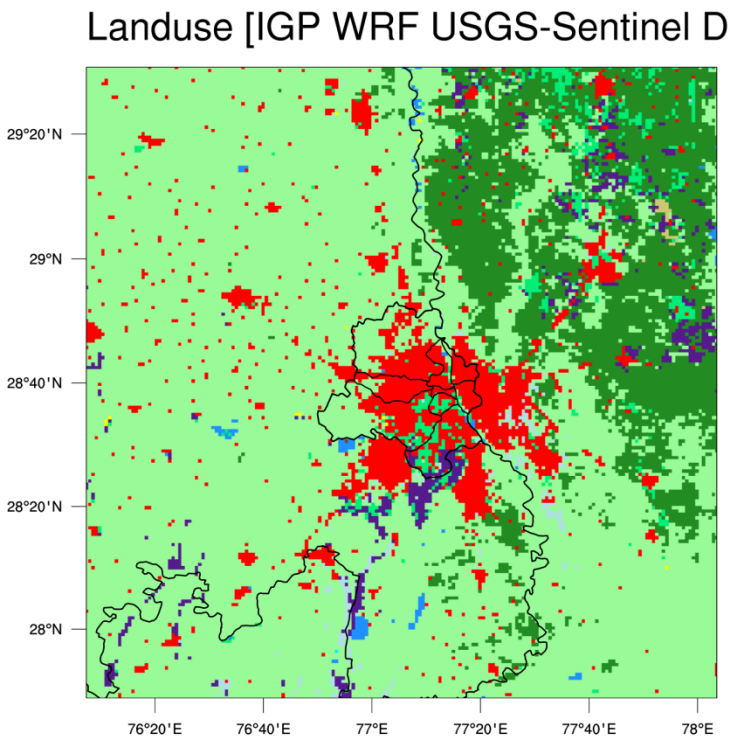

(c)

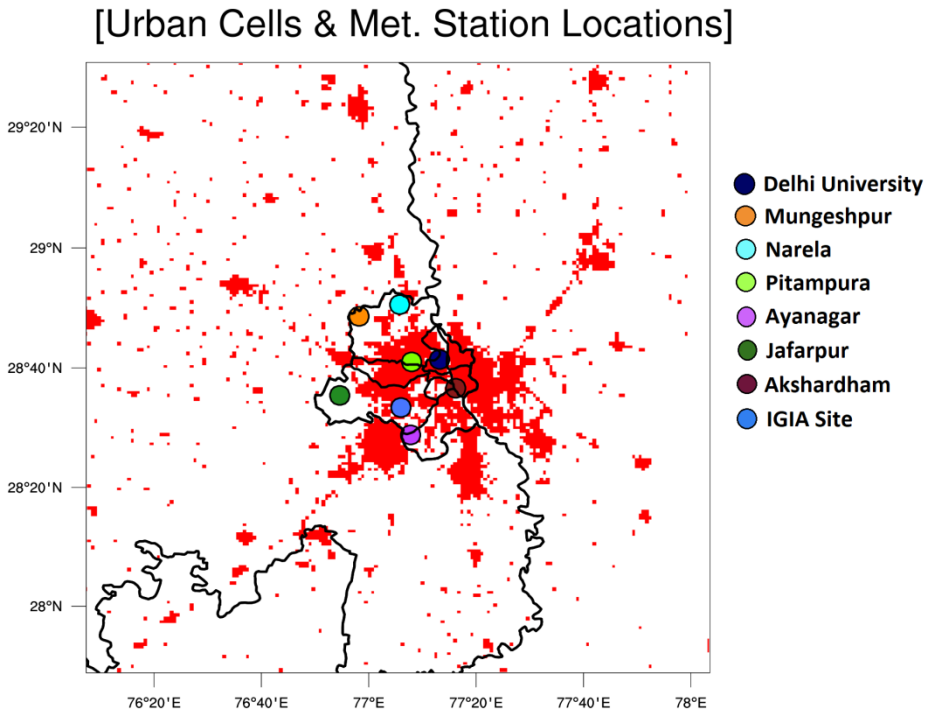

(d)

Figure 1. (a) Two nested domains setup over the Indo Gangetic Plain (IGP) region in Weather Research and Forecasting (WRF) model, (b-c) Updated USGS-Sentinel land-use and land-cover

(LULC) in Domain-1 (D1, 5-km grid spacing) and Domain-2 (D2, 1-km grid spacing), (d) Indian Meteorological Department (IMD) station locations (circular symbols) in Delhi urban region for verifying the model.

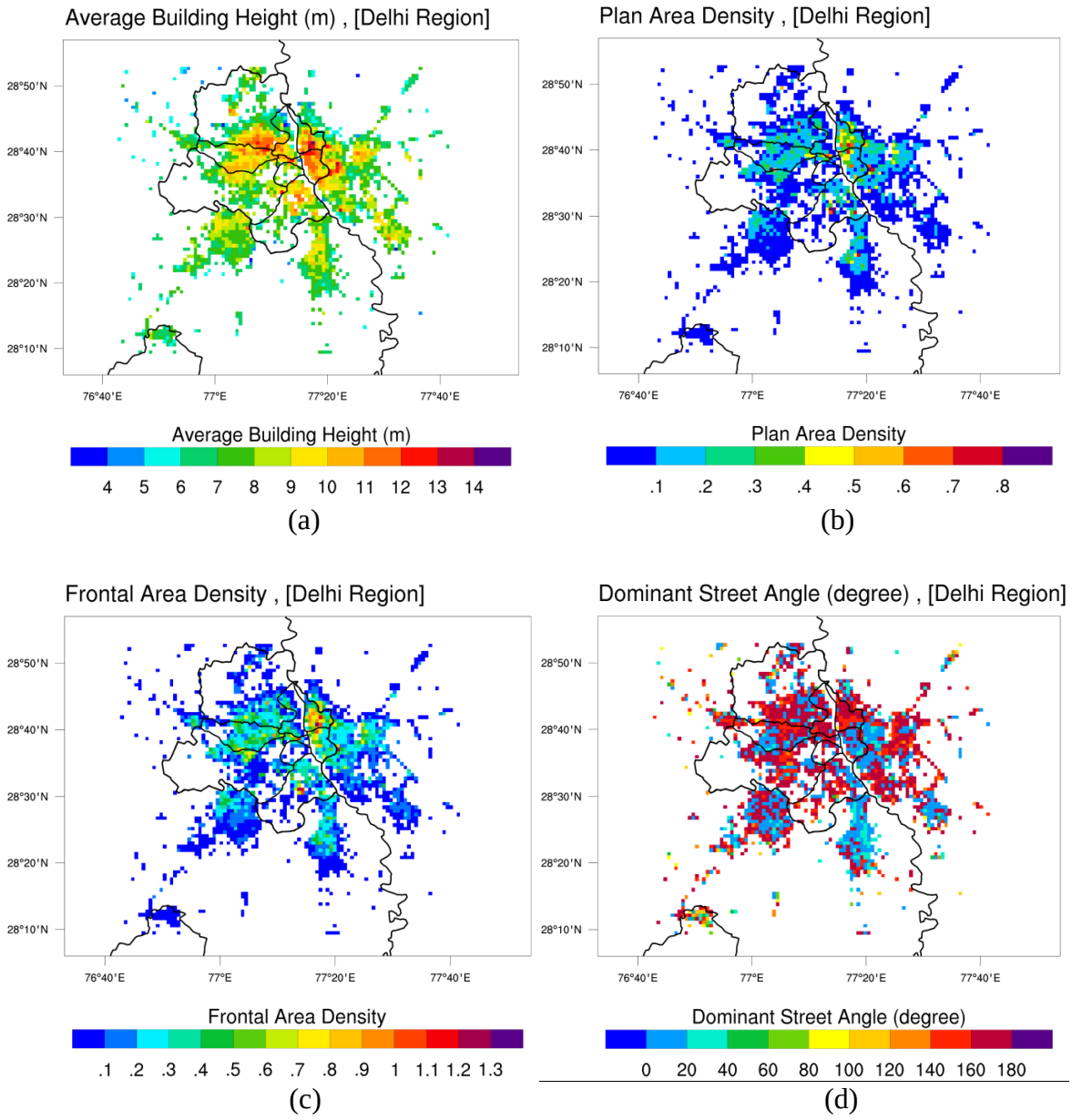

Figure 2. Delhi region urban morphological parameters dataset for (a) average building height [H], (b) plan area density [λ_p], (c) frontal area density [λ_f], and (d) street canyon orientation [φ].

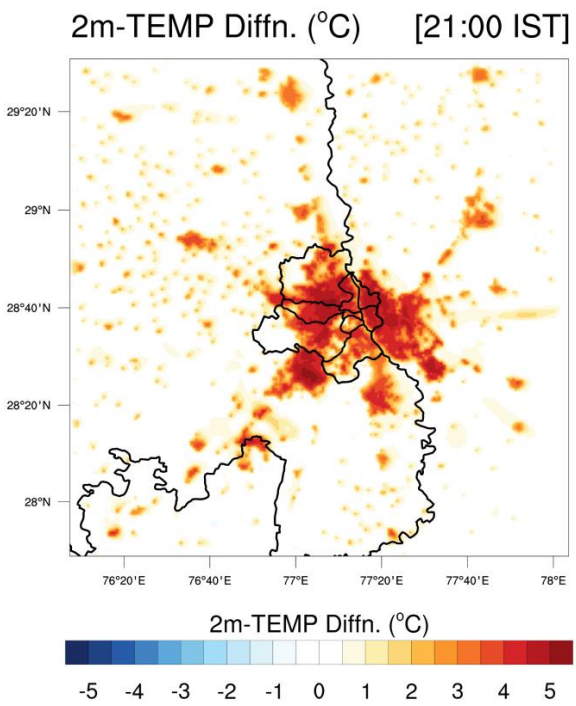
2m-TEMP Diffn. (°C) [21:00 IST]
29°20'N
29°N
28°40'N
28°20'N
28°N
76°20'E
76°40'E
77°E
77°20'E
77°40'E
78°E
2m-TEMP Diffn. (°C)
-5 -4 -3 -2 -1 0 1 2 3 4 5

(a)

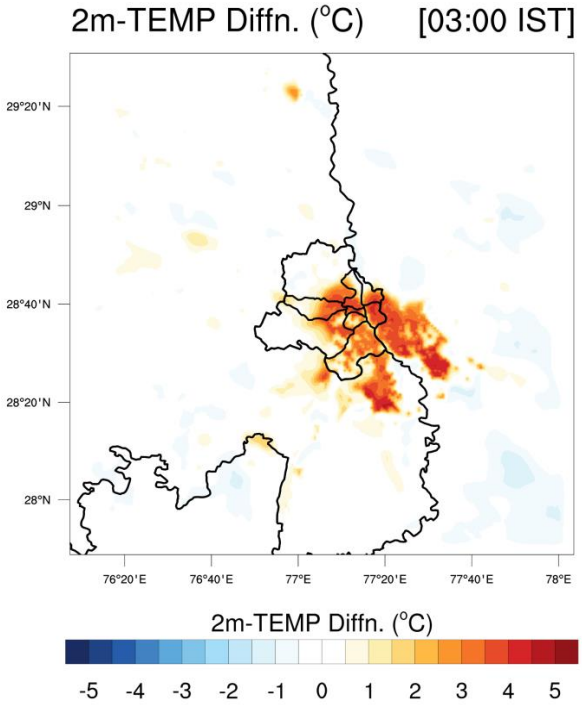
2m-TEMP Diffn. (°C) [03:00 IST]
29°20'N
29°N
28°40'N
28°20'N
28°N
76°20'E
76°40'E
77°E
77°20'E
77°40'E
78°E
2m-TEMP Diffn. (°C)
-5 -4 -3 -2 -1 0 1 2 3 4 5

(b)

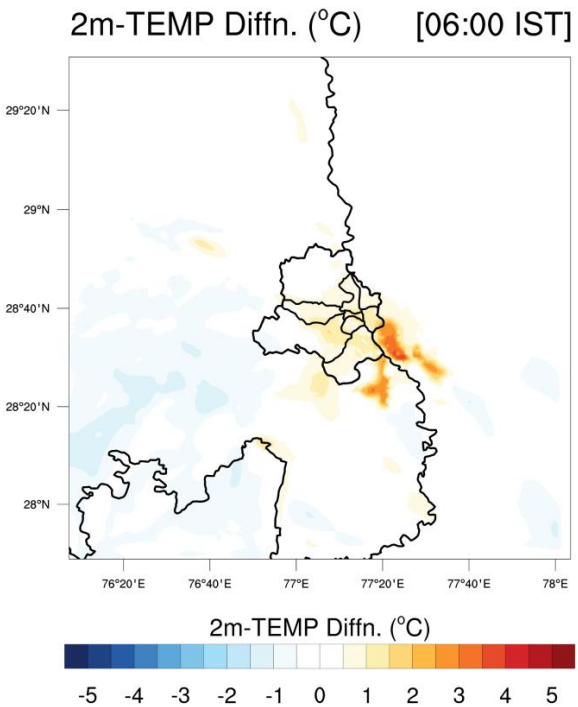
2m-TEMP Diffn. (°C) [06:00 IST]
29°20'N
29°N
28°40'N
28°20'N
28°N
76°20'E
76°40'E
77°E
77°20'E
77°40'E
78°E
2m-TEMP Diffn. (°C)
-5 -4 -3 -2 -1 0 1 2 3 4 5

(c)

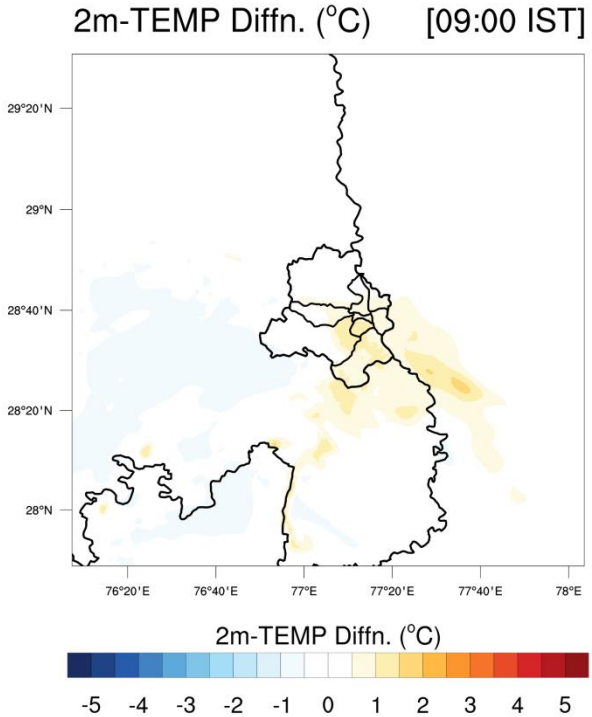
2m-TEMP Diffn. (°C) [09:00 IST]
29°20'N
29°N
28°40'N
28°20'N
28°N
76°20'E
76°40'E
77°E
77°20'E
77°40'E
78°E
2m-TEMP Diffn. (°C)
-5 -4 -3 -2 -1 0 1 2 3 4 5

(d)

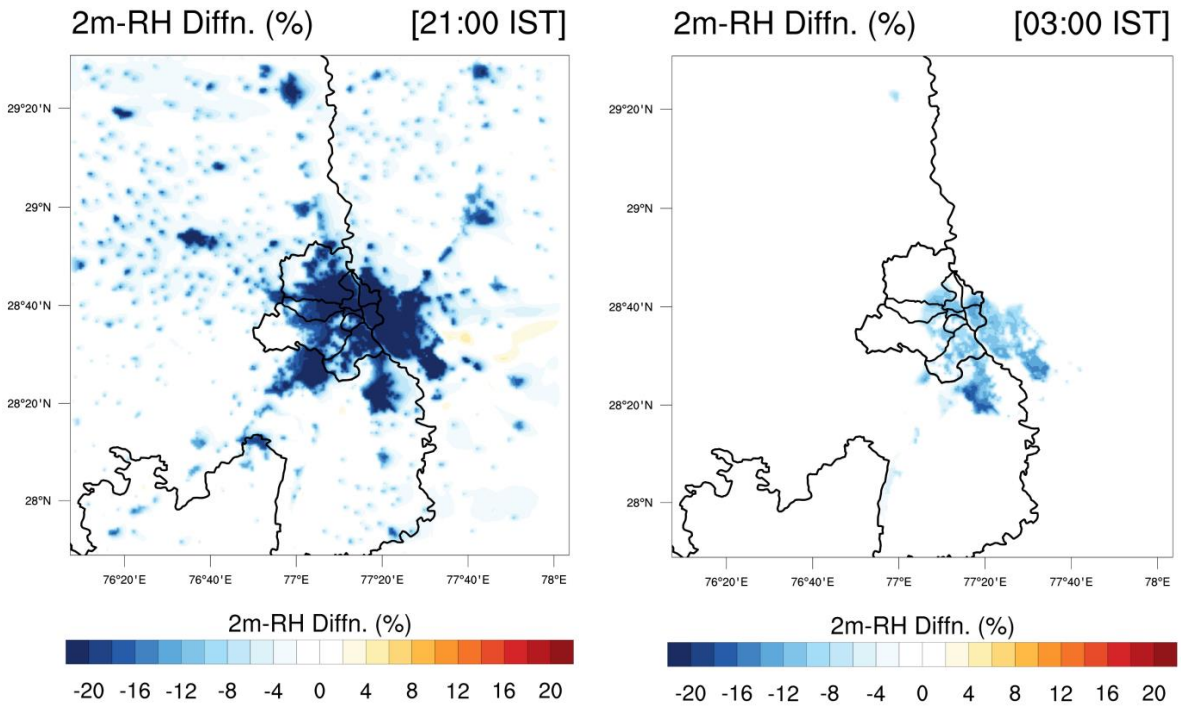
2m-RH Diffn. (%)
[21:00 IST]
29°20'N
29°N
28°40'N
28°20'N
28°N
76°20'E
76°40'E
77°E
77°20'E
77°40'E
78°E
2m-RH Diffn. (%)
-20 -16 -12 -8 -4 0 4 8 12 16 20
2m-RH Diffn. (%)
[03:00 IST]
29°20'N
29°N
28°40'N
28°20'N
28°N
76°20'E
76°40'E
77°E
77°20'E
77°40'E
78°E
2m-RH Diffn. (%)
-20 -16 -12 -8 -4 0 4 8 12 16 20

(e) (f)

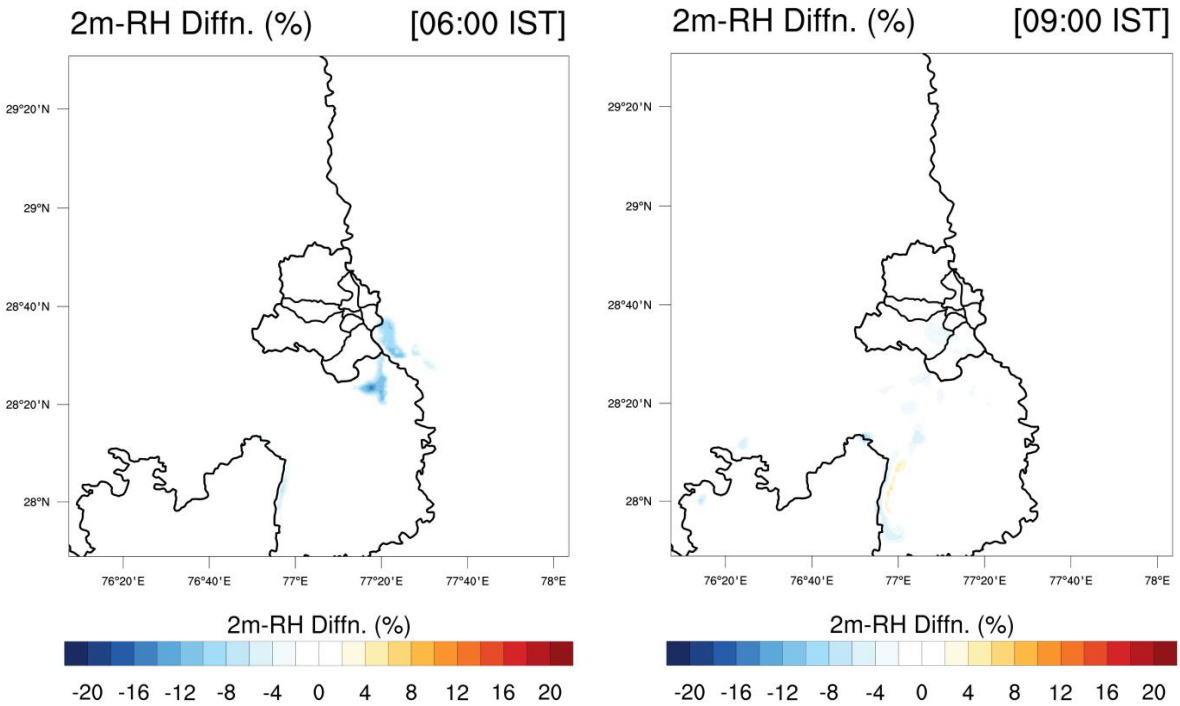
2m-RH Diffn. (%)
[06:00 IST]
29°20'N
29°N
28°40'N
28°20'N
28°N
76°20'E
76°40'E
77°E
77°20'E
77°40'E
78°E
2m-RH Diffn. (%)
-20 -16 -12 -8 -4 0 4 8 12 16 20
2m-RH Diffn. (%)
[09:00 IST]
29°20'N
29°N
28°40'N
28°20'N
28°N
76°20'E
76°40'E
77°E
77°20'E
77°40'E
78°E
2m-RH Diffn. (%)
-20 -16 -12 -8 -4 0 4 8 12 16 20

(g) (h)

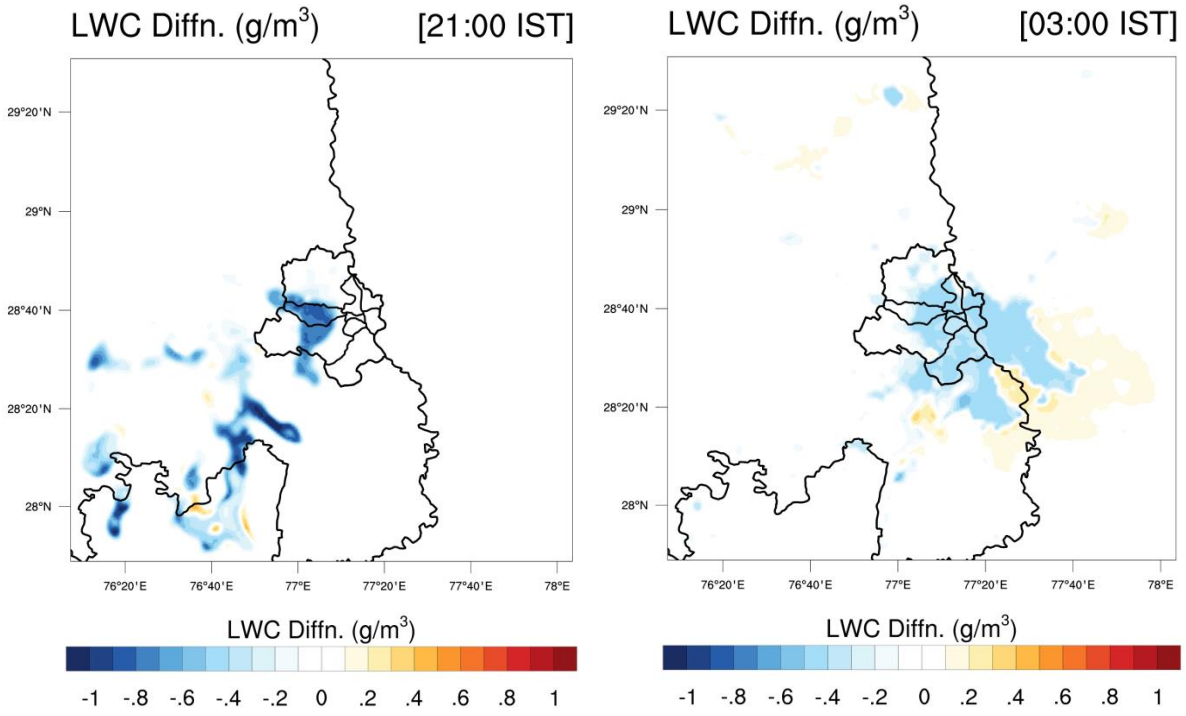
LWC Diffn. (g/m3) [21:00 IST]
LWC Diffn. (g/m3) [03:00 IST]
29°20'N
29°N
28°40'N
28°20'N
28°N
76°20'E
76°40'E
77°E
77°20'E
77°40'E
78°E
LWC Diffn. (g/m3)
-1 -.8 -.6 -.4 -.2 0 .2 .4 .6 .8 1

(i) (j)

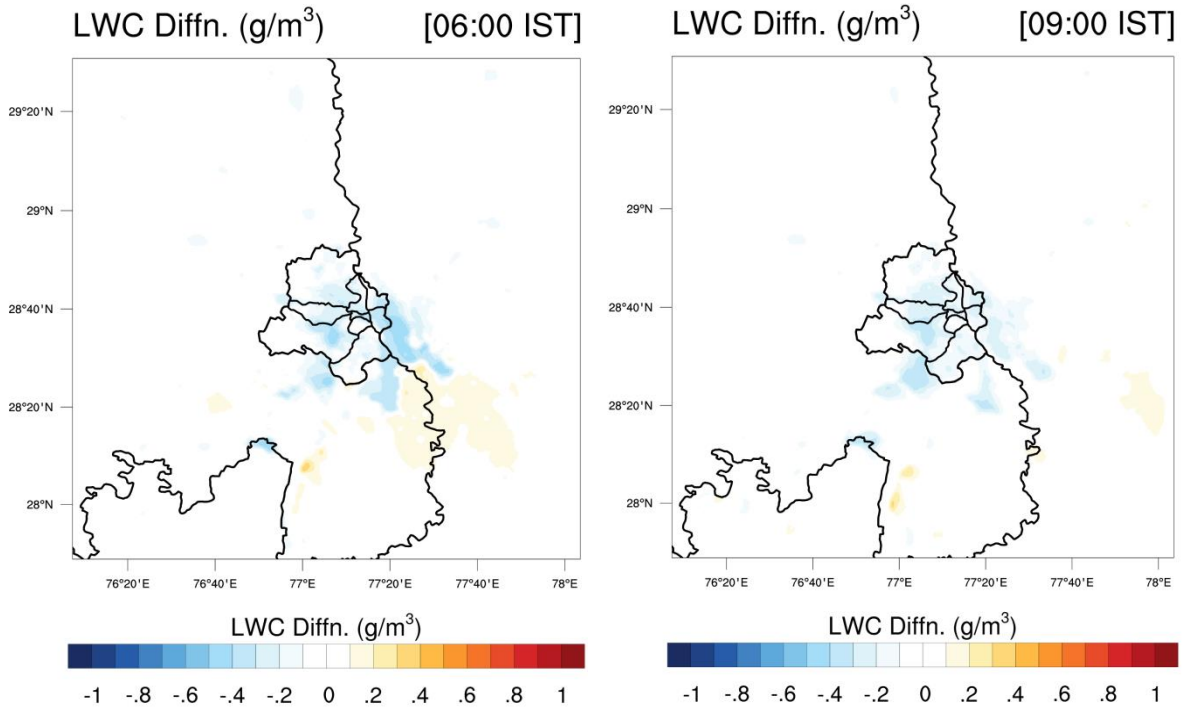
LWC Diffn. (g/m3) [06:00 IST]
LWC Diffn. (g/m3) [09:00 IST]
29°20'N
29°N
28°40'N
28°20'N
28°N
76°20'E
76°40'E
77°E
77°20'E
77°40'E
78°E
LWC Diffn. (g/m3)
-1 -.8 -.6 -.4 -.2 0 .2 .4 .6 .8 1

(k) (l)

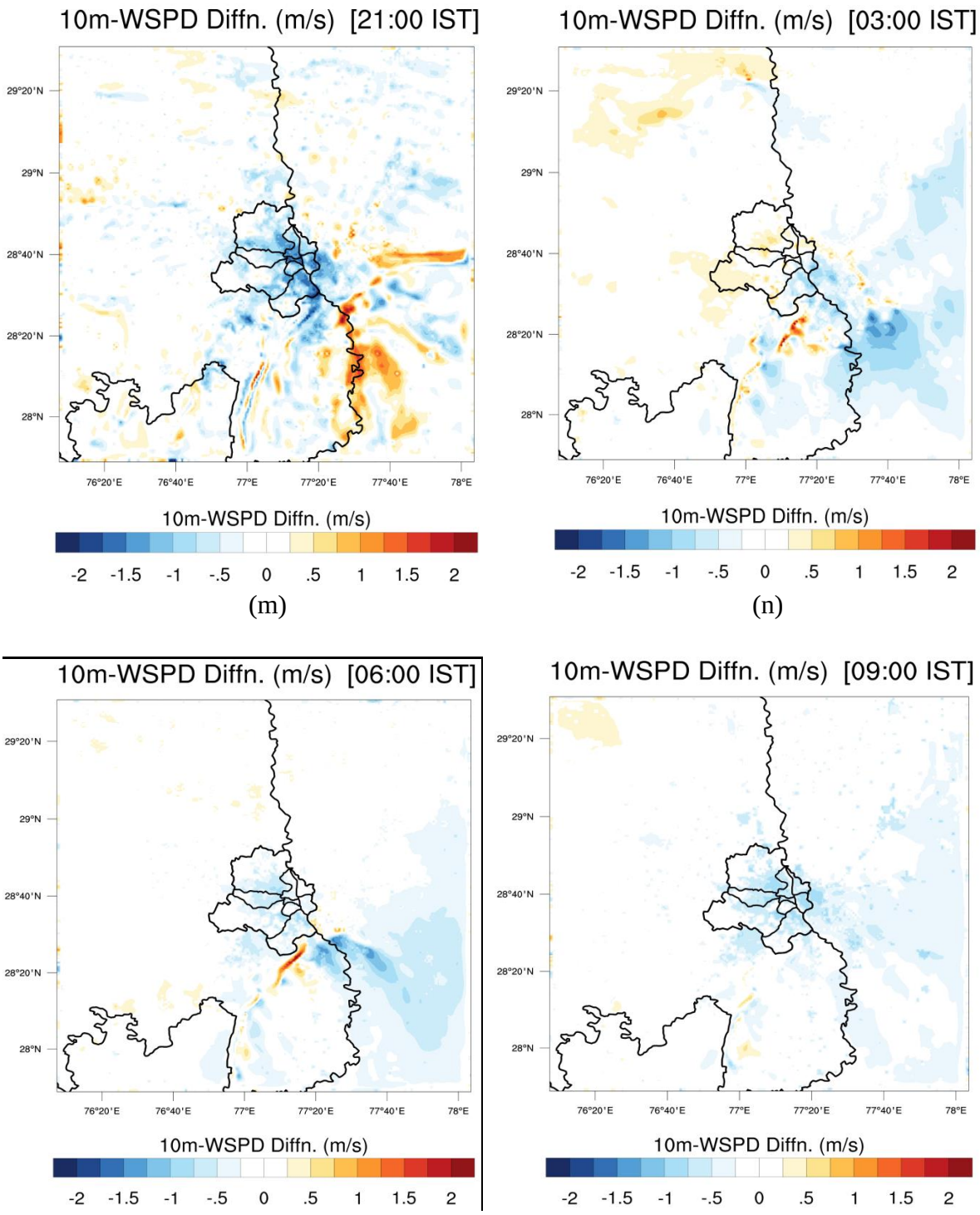

Figure 3. Contour plots of model difference [UACM – BACM] for (a-d) 2-m temperature, (e-h) 2-m relative humidity, (i-l) liquid water content at surface , and (m-p) 10-m wind speed during a fog event at 21:00 IST on 29 January 2017, and at 03:00 IST, 06:00 IST, 09:00 IST on 30 January 2017.

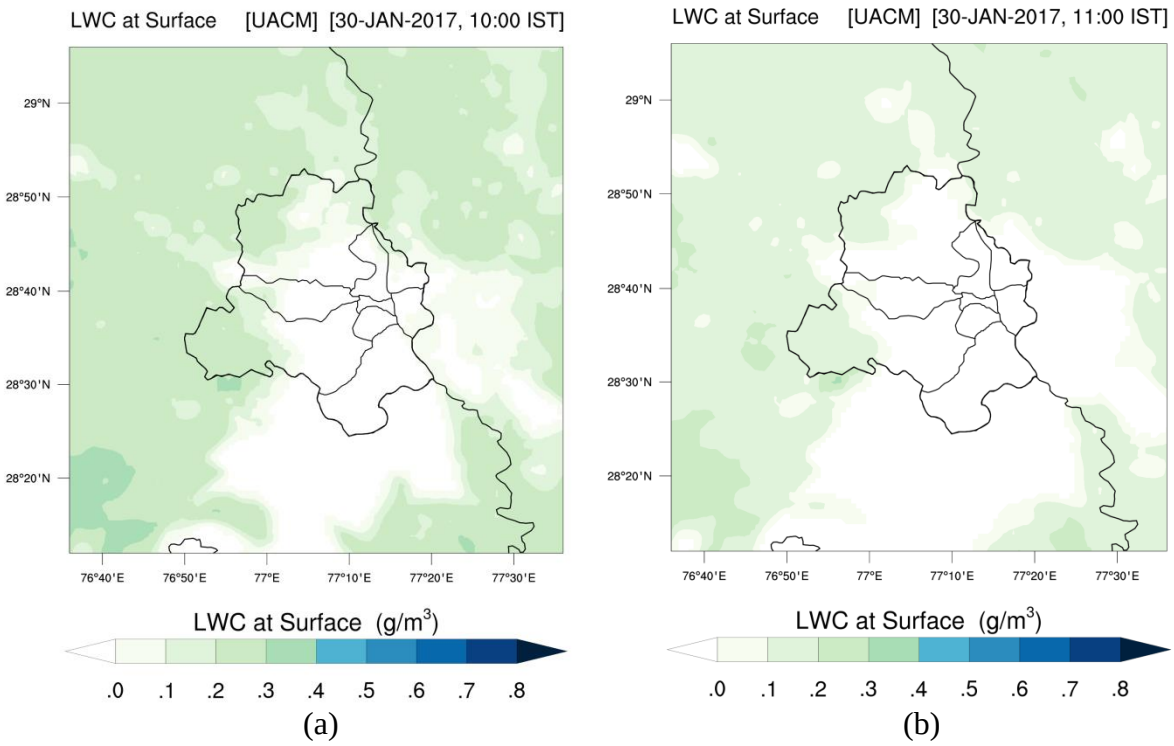

(a) (b)

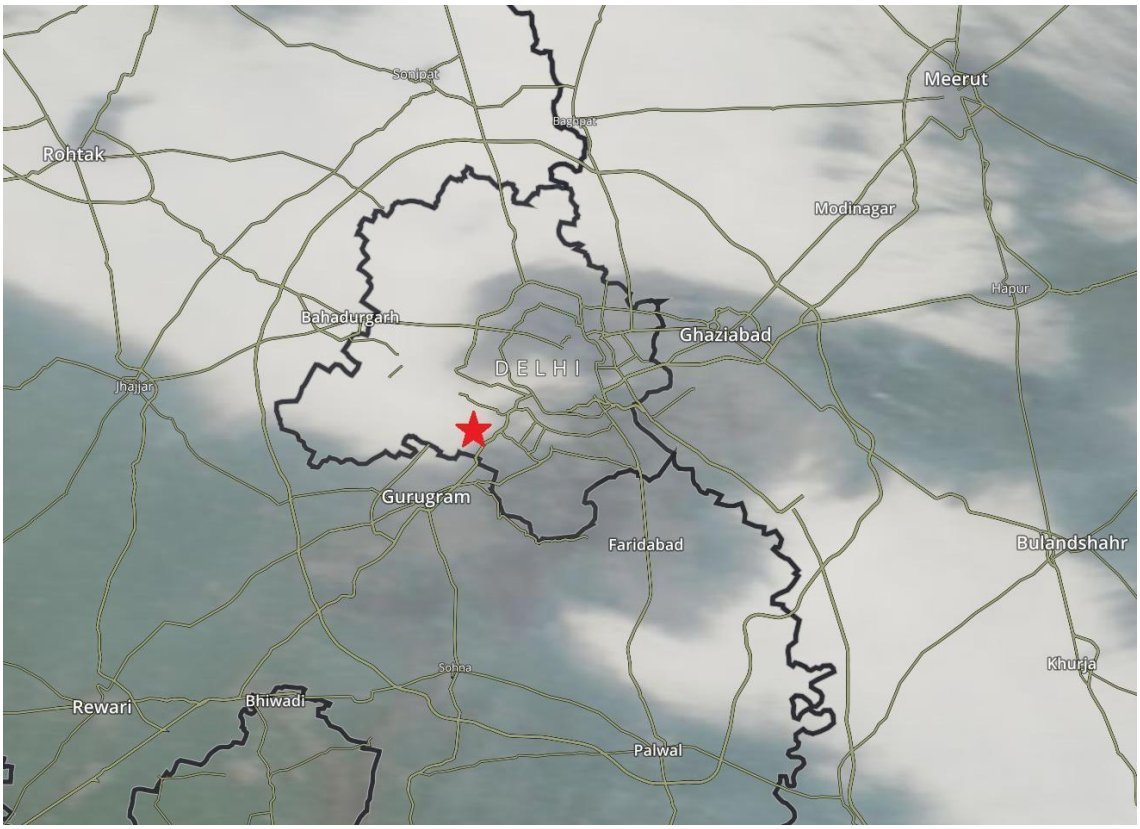

(c)

Figure 4. Contour plots of UACM liquid water content (LWC) at surface at (a) 10:00 IST, (b) 11:00 IST, and (c) a low cloud satellite image from NASA's MODIS (Moderate Resolution

Imaging Spectroradiometer) captured at approximately 10:30 am IST on January 30, 2017, during a fog event over the Delhi region. The 'red star' symbol marks the location of the Delhi Indira Gandhi International Airport (IGIA) at 28.5562º N, 77.100º E.

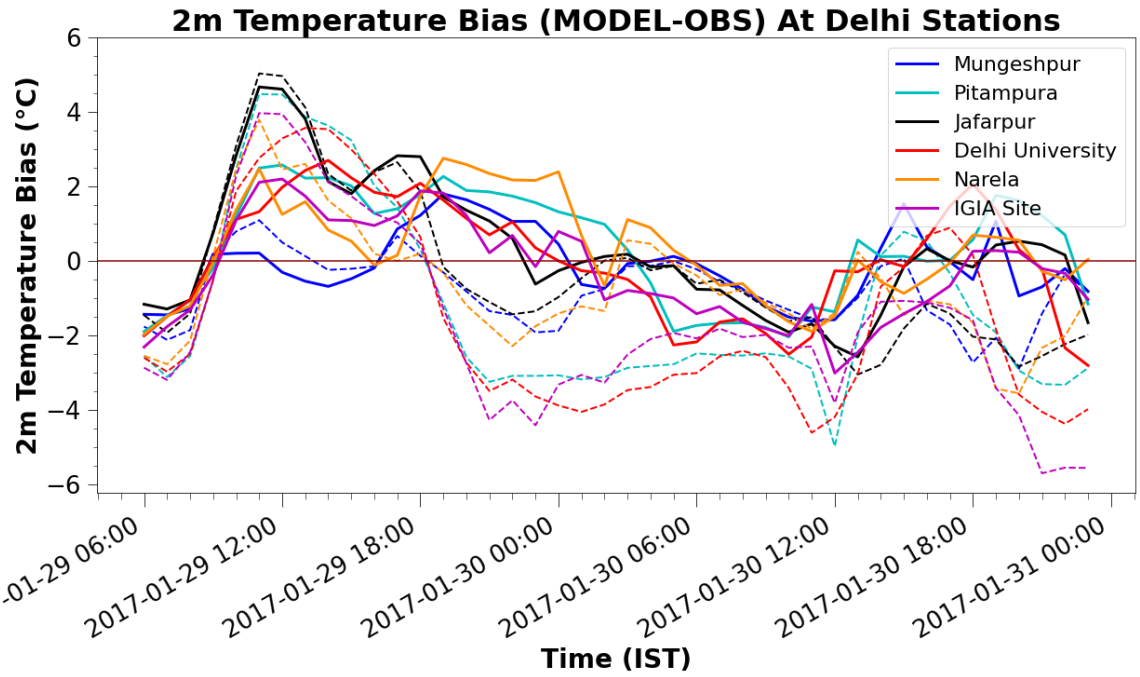

(a)

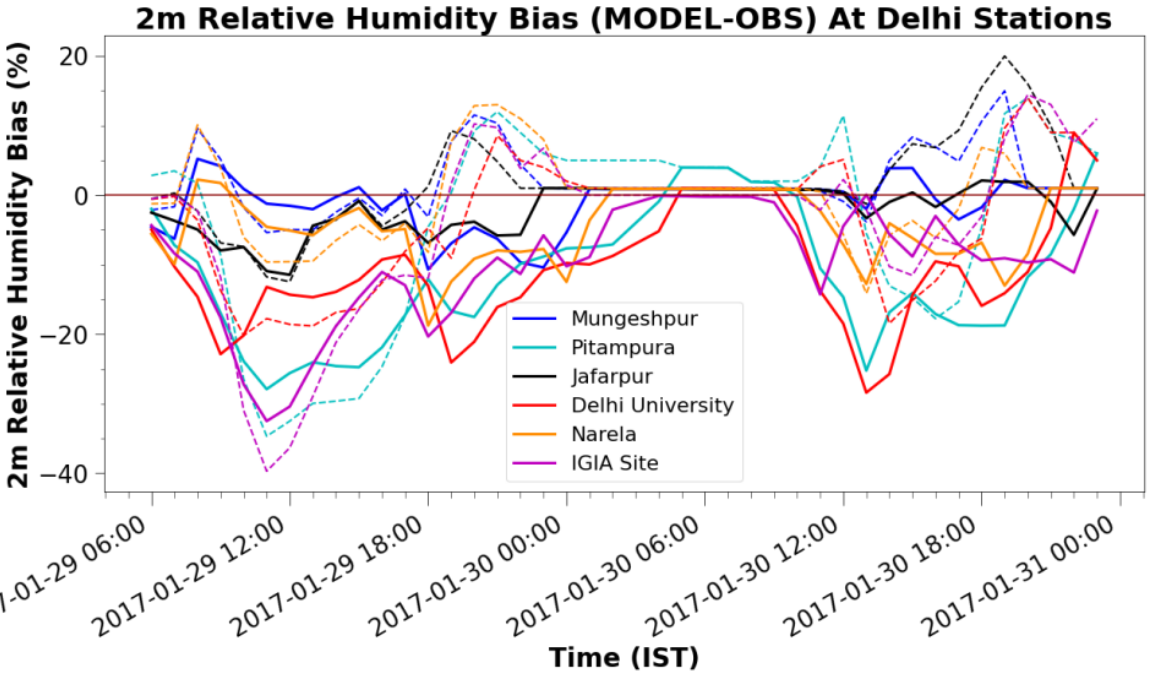

(b)

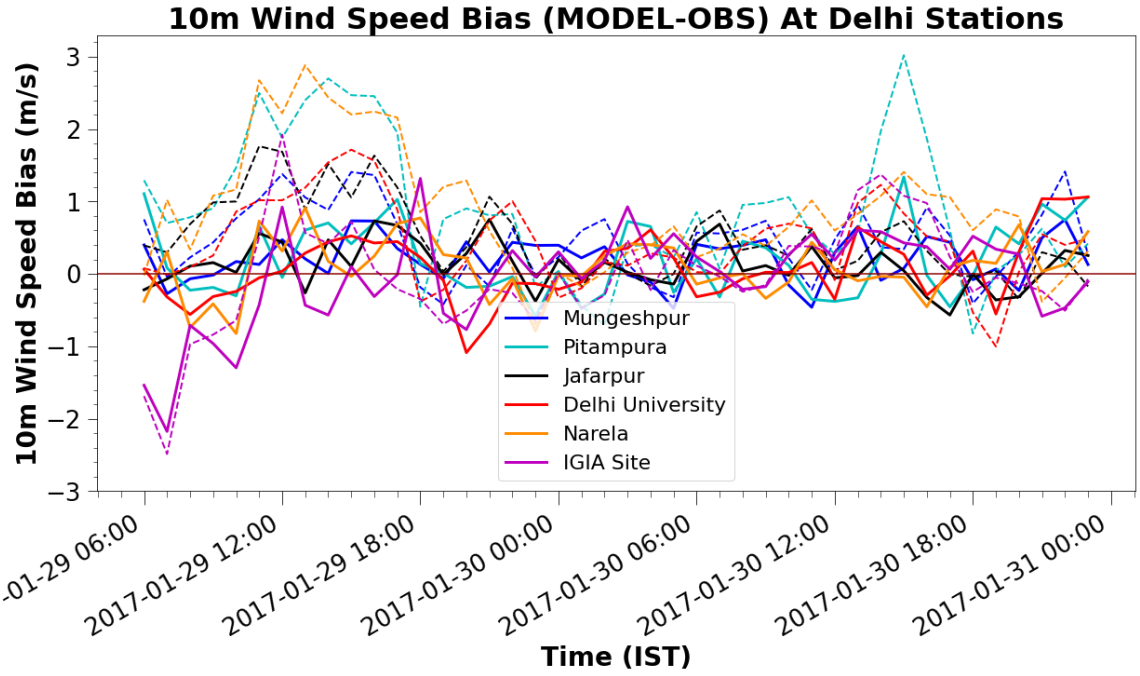
10m Wind Speed Bias (MODEL-OBS) At Delhi Stations
10m Wind Speed Bias (m/s)
3
2
1
0
−1
−2
−3
Mungeshpur
Pitampura
Jafarpur
Delhi University
Narela
IGIA Site
2017-01-29 06:00
2017-01-29 12:00
2017-01-29 18:00
2017-01-30 00:00
2017-01-30 06:00
2017-01-30 12:00
2017-01-30 18:00
2017-01-31 00:00
Time (IST)

(c)

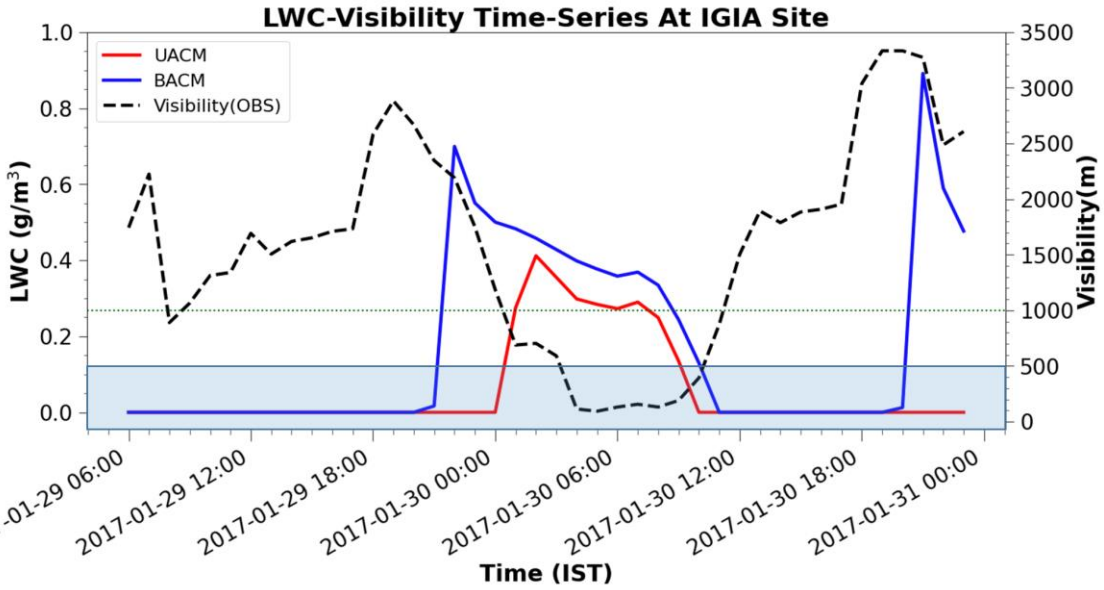
LWC-Visibility Time-Series At IGIA Site
UACM
BACM
Visibility(OBS)
LWC (g/m³)
1.0
0.8
0.6
0.4
0.2
0.0
Visibility(m)
3500
3000
2500
2000
1500
1000
500
0
2017-01-29 06:00
2017-01-29 12:00
2017-01-29 18:00
2017-01-30 00:00
2017-01-30 06:00
2017-01-30 12:00
2017-01-30 18:00
2017-01-31 00:00
Time (IST)

(d)

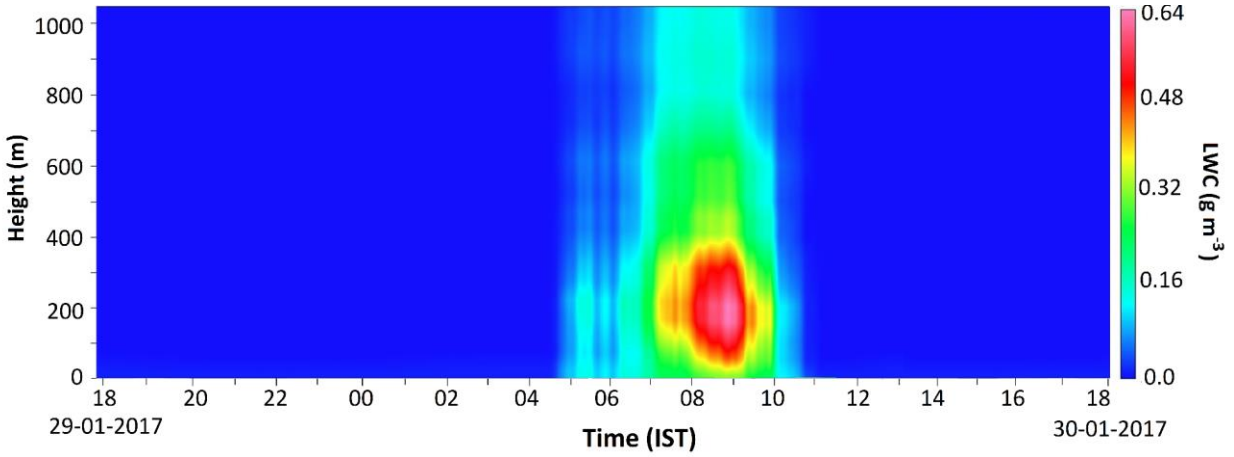

(e)

Figure 5. Time-series bias plots [MODEL – OBS] (bold line: UACM, dashed line: BACM) for (a) 2-m temperature, (b) 2-m relative humidity, (c) 10-m wind speed at Delhi urban Indian Meteorological Department (IMD) stations, (d) time-series comparison of models liquid water content (LWC) at the surface with visibility data at the Indira Gandhi International Airport (IGIA) site from 29-Jan-2017 (06:00 IST) to 30-Jan-2017 (23:00 IST), and (e) radiometer LWC observations at the IGIA site during a fog event case. UACM: Urban Asymmetric Convective Model; BACM: Base Asymmetric Convective Model (WRF model control runs); OBS: Observations.

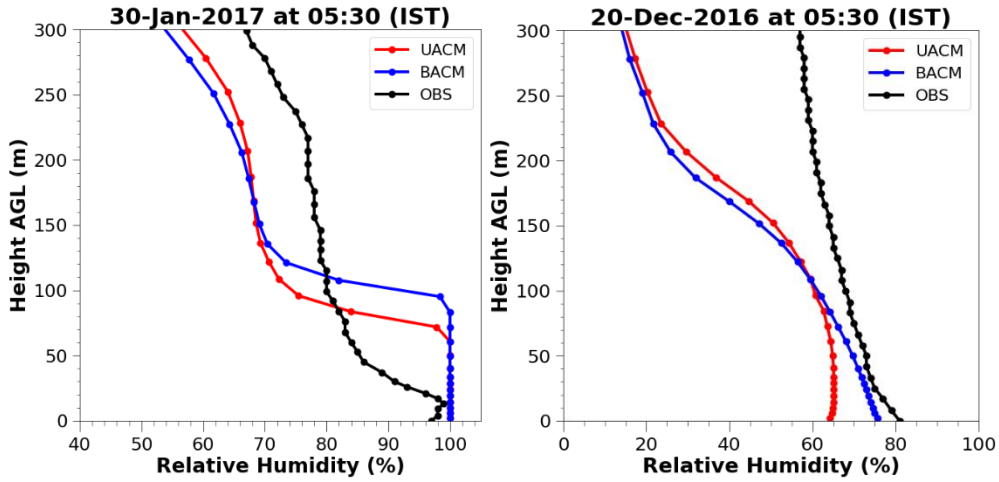

(a) (d)

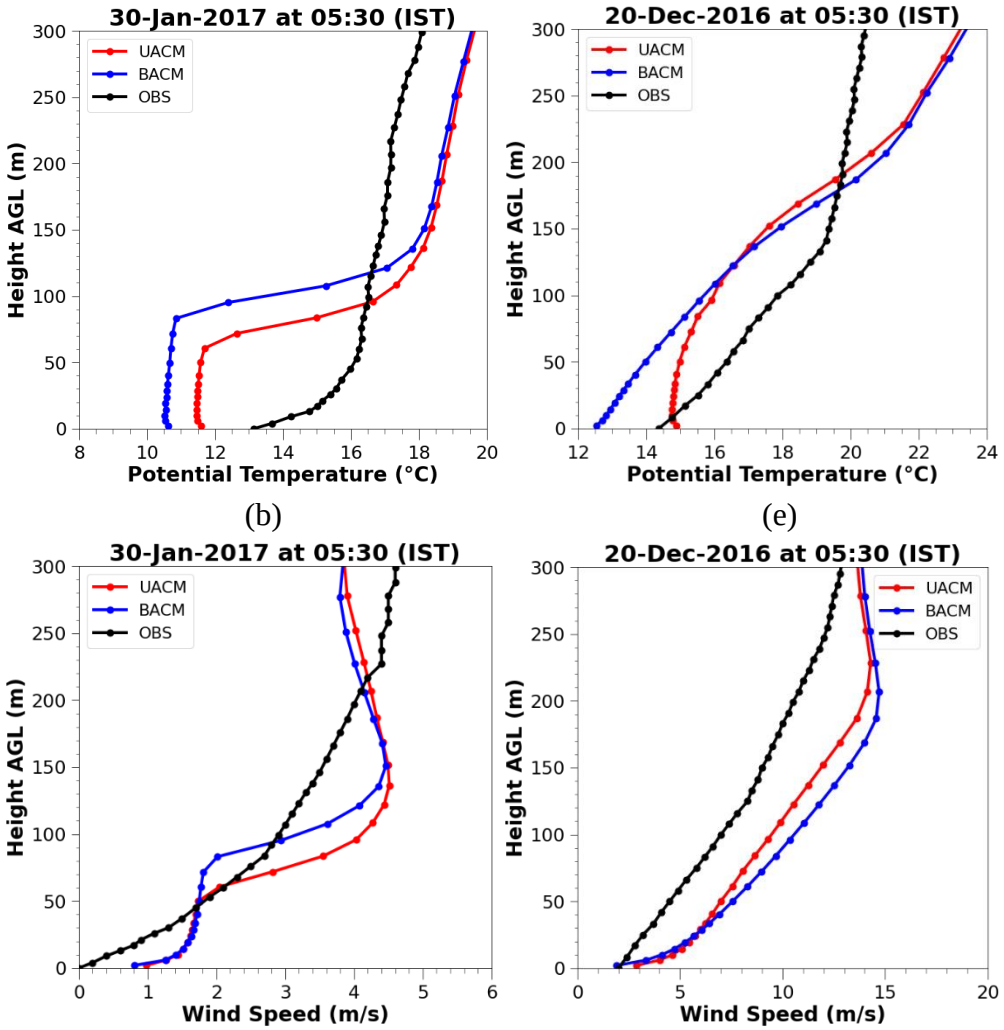

Figure 6. Vertical profiles of (a) relative humidity, (b) potential temperature, (c) horizontal wind speed on 30-Jan-2017 (05:30 IST) during a fog event case; and (d) relative humidity, (e) potential temperature, (f) horizontal wind speed on 20-Dec-2016 (05:30 IST) during a clear sky case at Ayanagar meteorological (IMD) station. UACM: Urban Asymmetric Convective Model; BACM: Base Asymmetric Convective Model (WRF model control runs); OBS: Observations.

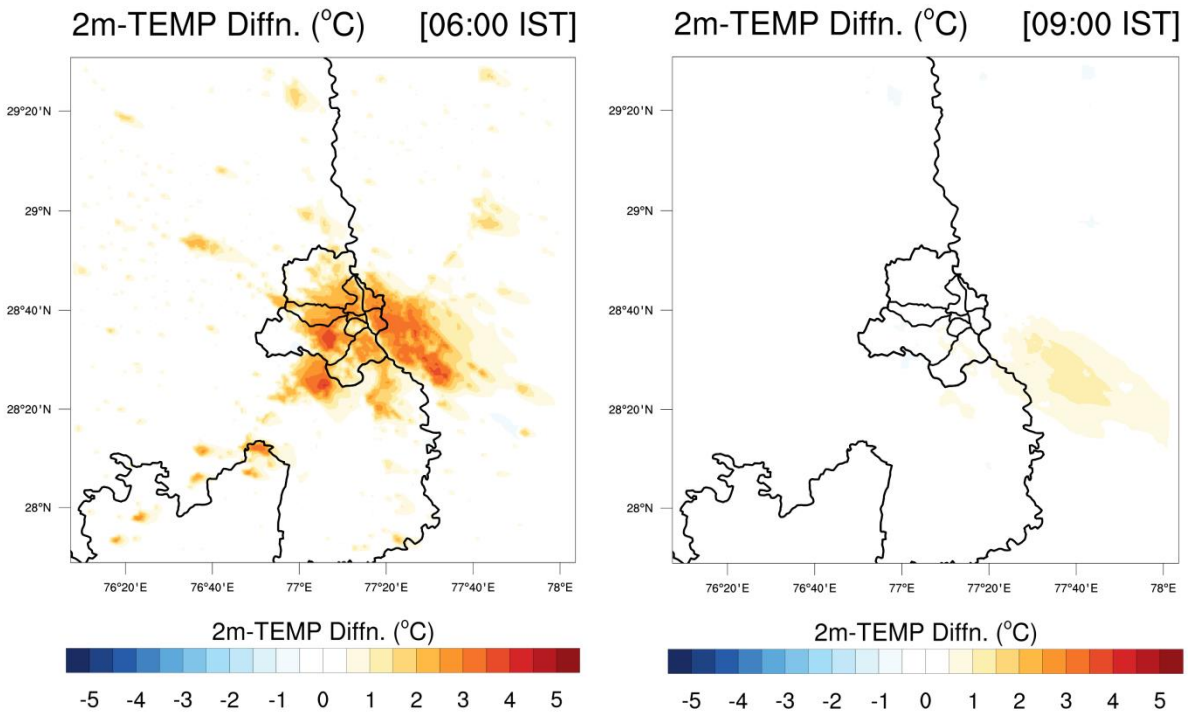
2m-TEMP Diffn. (°C) [06:00 IST]
2m-TEMP Diffn. (°C) [09:00 IST]
29°20'N
29°N
28°40'N
28°20'N
28°N
76°20'E
76°40'E
77°E
77°20'E
77°40'E
78°E
2m-TEMP Diffn. (°C)
-5 -4 -3 -2 -1 0 1 2 3 4 5

(a) (b)

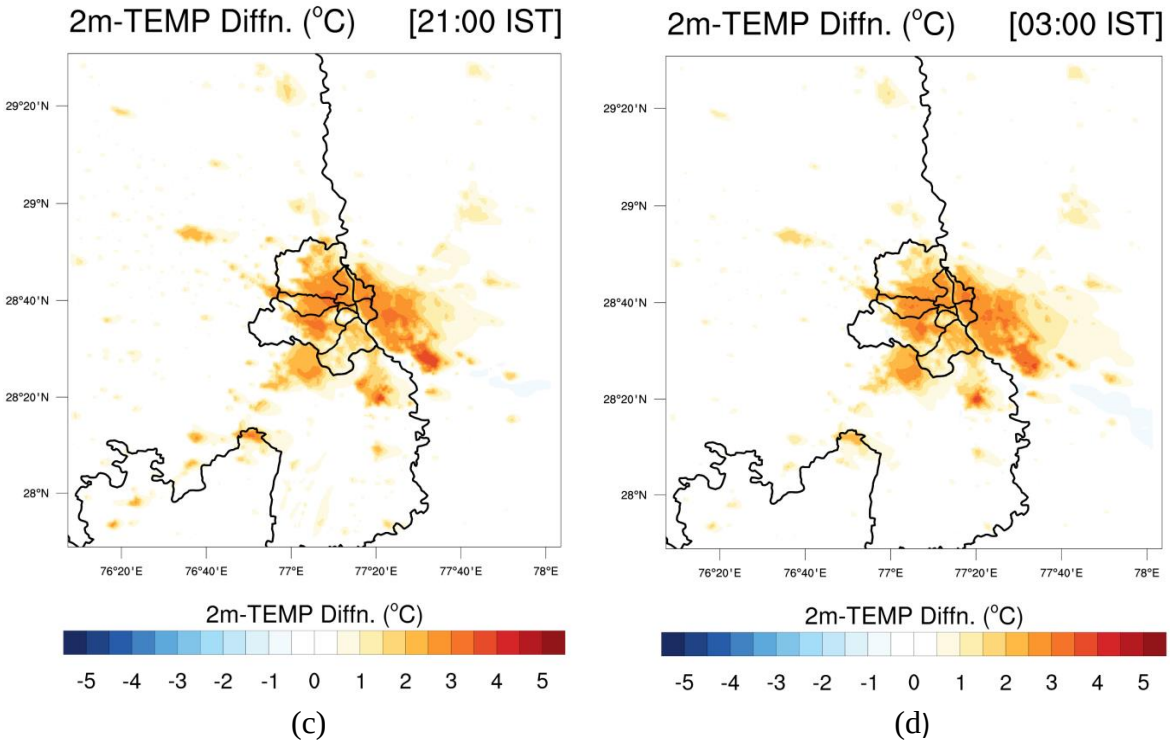
2m-TEMP Diffn. (°C) [21:00 IST]
2m-TEMP Diffn. (°C) [03:00 IST]
29°20'N
29°N
28°40'N
28°20'N
28°N
76°20'E
76°40'E
77°E
77°20'E
77°40'E
78°E
2m-TEMP Diffn. (°C)
-5 -4 -3 -2 -1 0 1 2 3 4 5

(c) (d)

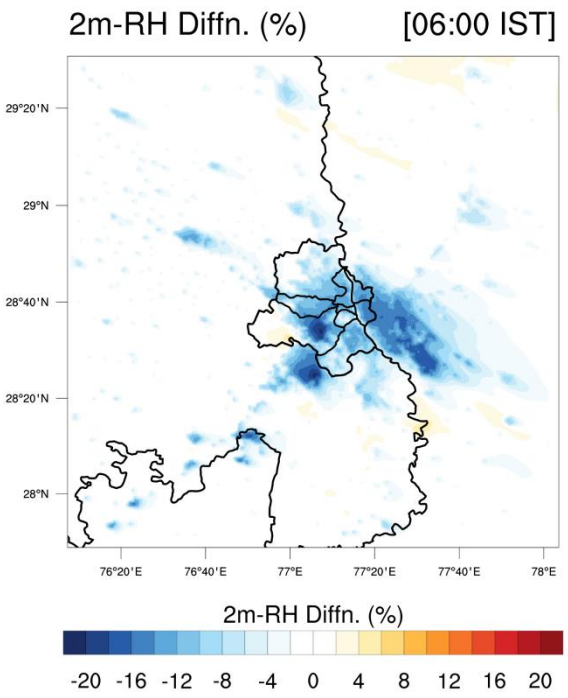
2m-RH Diffn. (%)
[06:00 IST]
29°20'N
29°N
28°40'N
28°20'N
28°N
76°20'E
76°40'E
77°E
77°20'E
77°40'E
78°E
2m-RH Diffn. (%)
-20 -16 -12 -8 -4 0 4 8 12 16 20

(e)

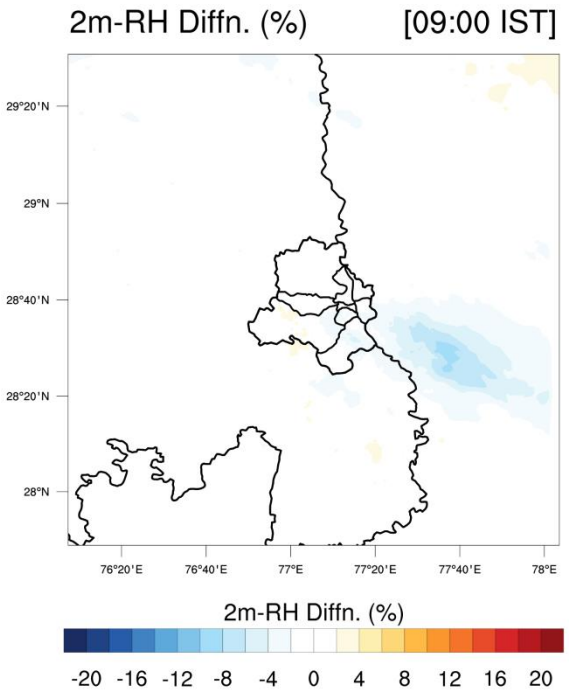
2m-RH Diffn. (%)
[09:00 IST]
29°20'N
29°N
28°40'N
28°20'N
28°N
76°20'E
76°40'E
77°E
77°20'E
77°40'E
78°E
2m-RH Diffn. (%)
-20 -16 -12 -8 -4 0 4 8 12 16 20

(f)

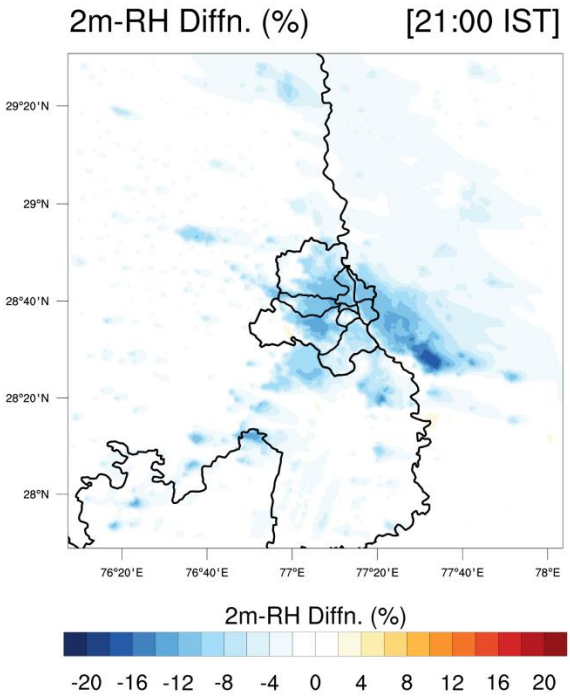
2m-RH Diffn. (%)
[21:00 IST]
29°20'N
29°N
28°40'N
28°20'N
28°N
76°20'E
76°40'E
77°E
77°20'E
77°40'E
78°E
2m-RH Diffn. (%)
-20 -16 -12 -8 -4 0 4 8 12 16 20

(g)

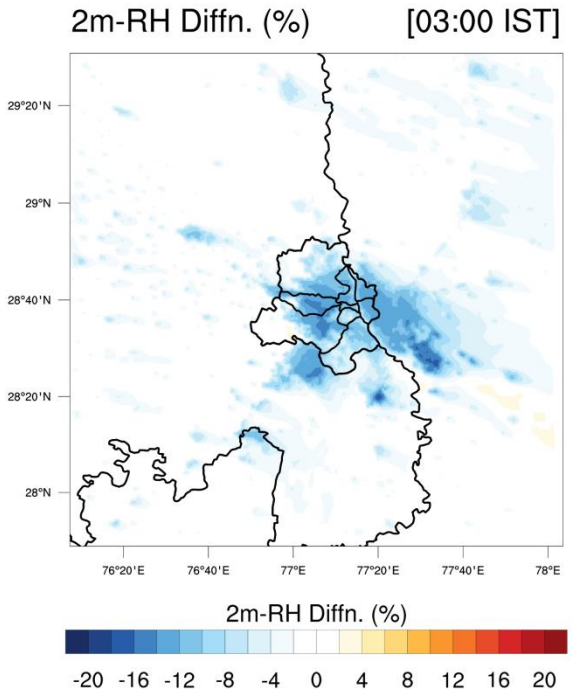
2m-RH Diffn. (%)
[03:00 IST]
29°20'N
29°N
28°40'N
28°20'N
28°N
76°20'E
76°40'E
77°E
77°20'E
77°40'E
78°E
2m-RH Diffn. (%)
-20 -16 -12 -8 -4 0 4 8 12 16 20

(h)

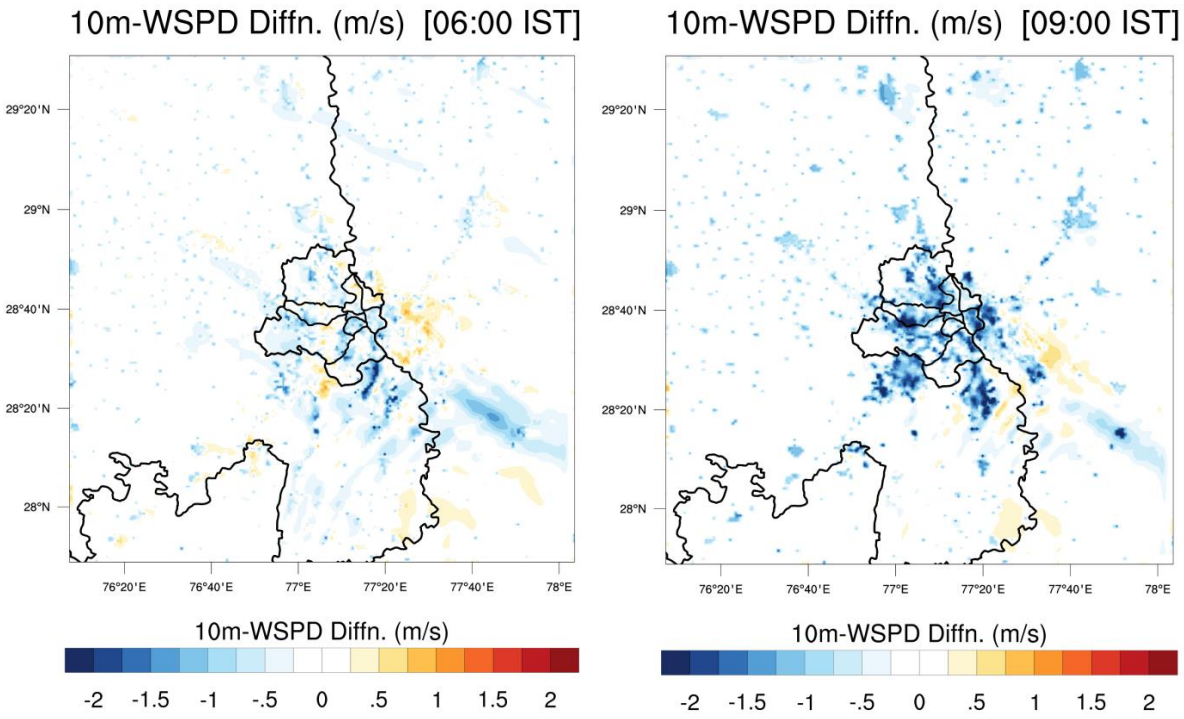
10m-WSPD Diffn. (m/s) [06:00 IST]
10m-WSPD Diffn. (m/s) [09:00 IST]
29°20'N
29°N
28°40'N
28°20'N
28°N
76°20'E
76°40'E
77°E
77°20'E
77°40'E
78°E
10m-WSPD Diffn. (m/s)
-2 -1.5 -1 -.5 0 .5 1 1.5 2

(i) (j)

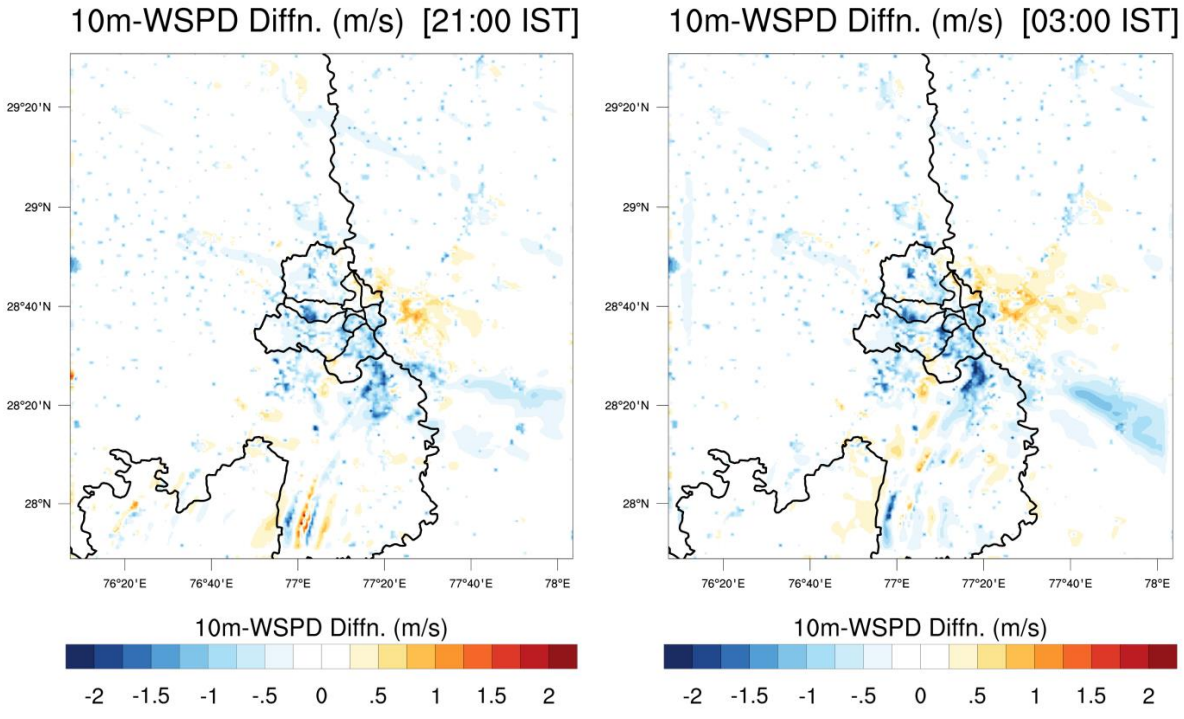
10m-WSPD Diffn. (m/s) [21:00 IST]
10m-WSPD Diffn. (m/s) [03:00 IST]
29°20'N
29°N
28°40'N
28°20'N
28°N
76°20'E
76°40'E
77°E
77°20'E
77°40'E
78°E
10m-WSPD Diffn. (m/s)
-2 -1.5 -1 -.5 0 .5 1 1.5 2

(k) (l)

Figure 7. Contour plots of model difference [UACM – BACM] for (a-d) 2-m temperature, (e-h) 2-m relative humidity, and (i-l) 10-m wind speed during a clear sky case at 06:00 IST, 09:00 IST, 21:00 IST, and 03:00 IST on 20-Dec-2016.

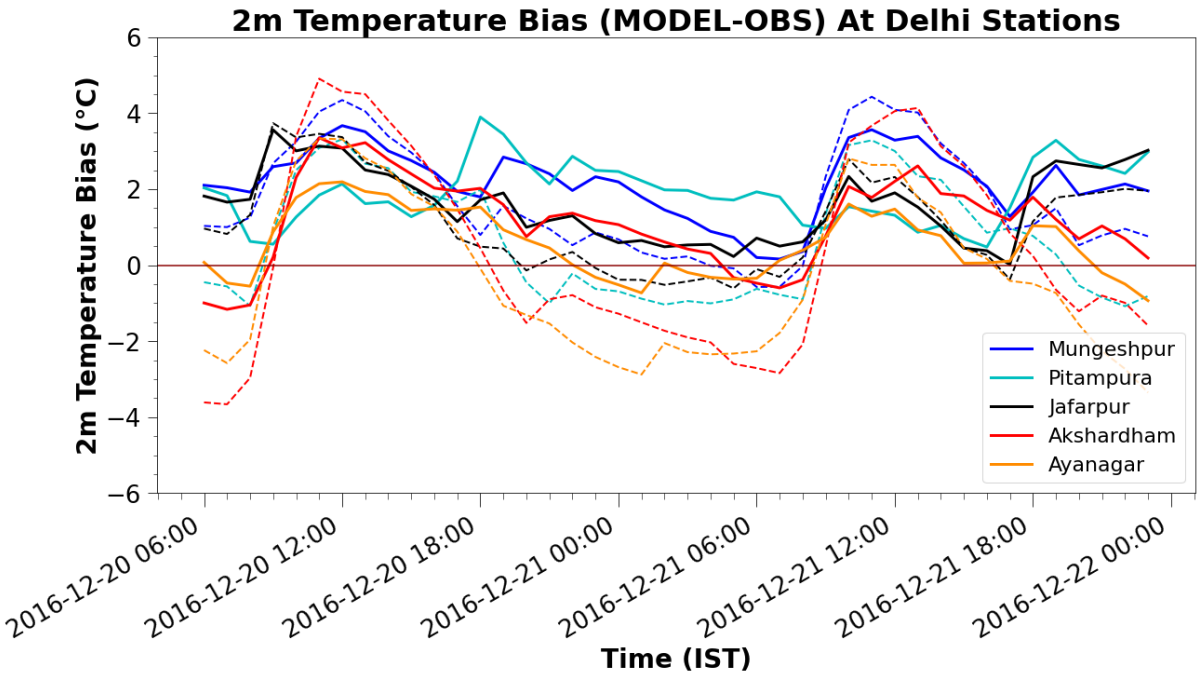

(a)

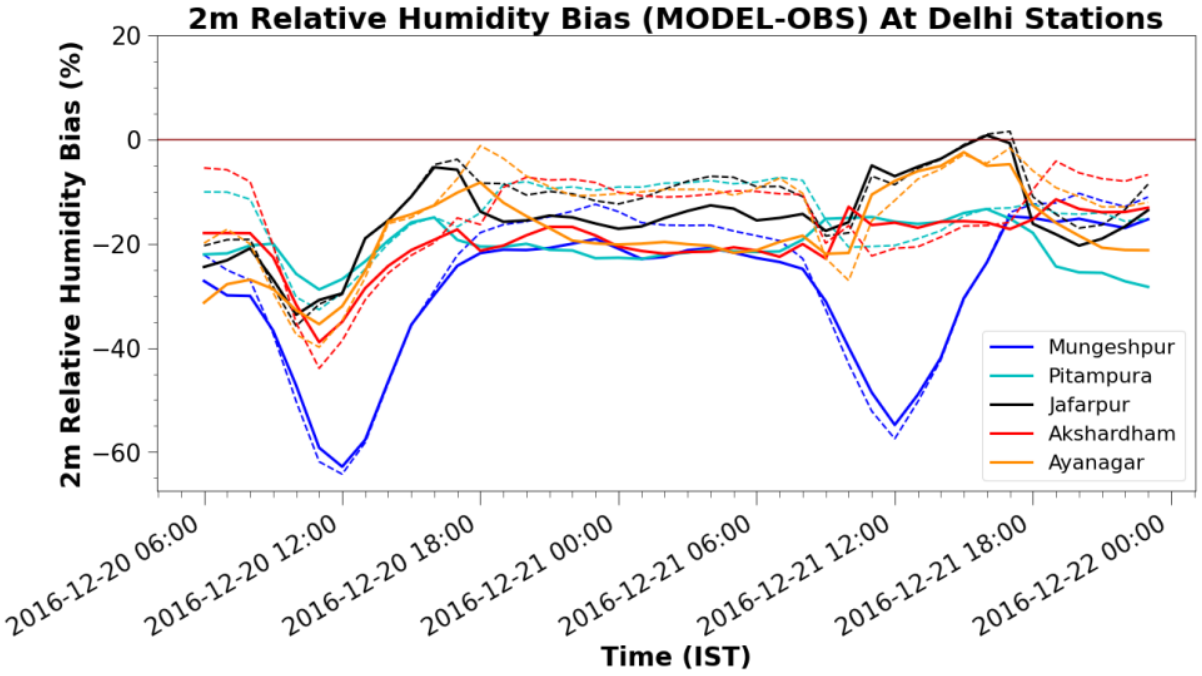

(b)

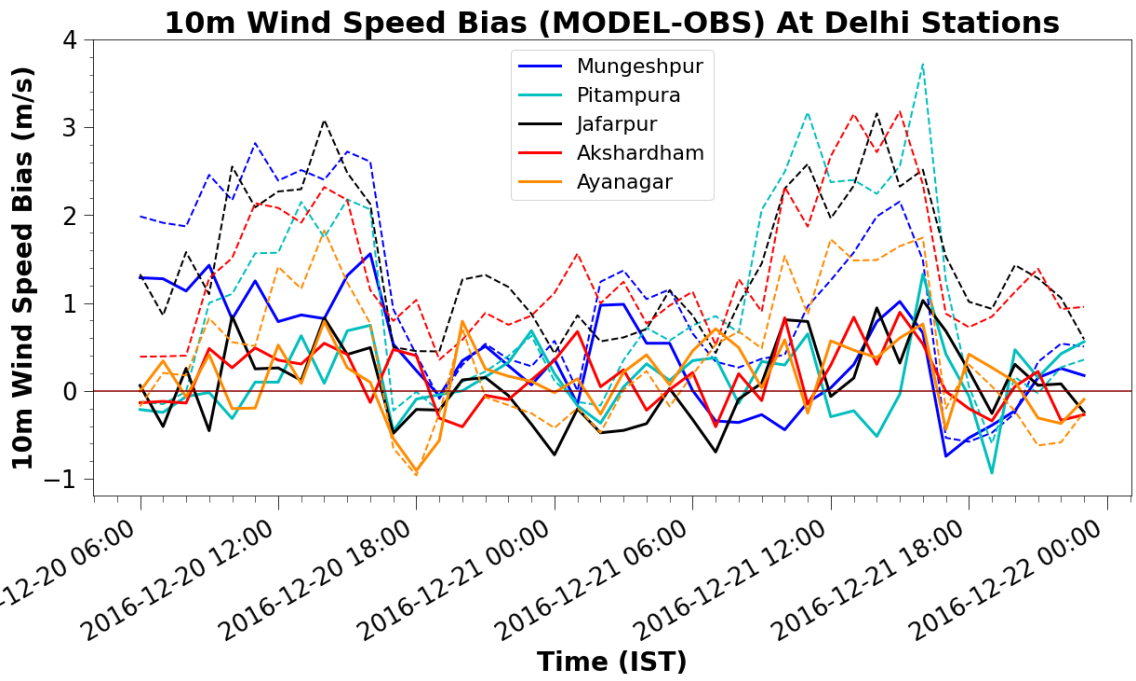

(c)

Figure 8. Time-series bias plots [MODEL – OBS] (bold line: UACM, dashed line: BACM) for (a) 2-m temperature, (b) 2-m relative humidity, (c) 10-m wind speed at Delhi urban Indian Meteorological Department (IMD) stations during a clear sky case from 20-Dec-2016 (06:00 IST) to 21-Dec-2016 (23:00 IST).

Tables

Table 1. Configuration settings used in the Weather Research and Forecasting (WRF) Model V3.8

WRF V3.8 schemes and other options	Selected configuration
Vertical sigma levels	54
Model top pressure	50 hPa (~20-km AGL)
Meteorological data (initial conditions)	National Centers for Environmental Prediction Final (Final Operational Global Analysis data) with a spatial resolution of 1° in latitude and longitude, and a temporal resolution of 6 h
Nested domain grid spacing	D1 (5 km), D2 (1 km)
Domain grid points	D1 (440 × 200), D2 (191 × 191)
Microphysics	WRF single-moment 6-class [WSM6] graupel scheme (D1-D2)
Longwave radiation	CAM LW scheme (D1-D2)
Shortwave radiation	CAM SW scheme (D1-D2)
Surface clay physics	Pleim-Xiu (PX) (D1-D2)
Surface physics	Pleim-Xiu (PX) scheme (D1), New Urban-PX scheme only at D2
Planetary boundary layer physics	Base-ACM2 (Pleim) scheme (D1) [BACM], New Urban-ACM2 [UACM] scheme only at D2
Cumulus physics	OFF (D1-D2)
No. of soil layers	2 (for PX)
No. of land categories	24 (USGS)
Nesting	One-way nesting
Coarse domain time step	8 s (with 1:4 parent time-step ratio)
No. of metgrid levels	27
No. of metgrid soil levels	4
Surface urban physics	OFF (D1-D2)

Note: ACM2 = Asymmetric Convective Model Version-2; BACM = Base Asymmetric Convective Model; UACM = Urban Asymmetric Convective Model.

966 **Table 2.** Statistical Metrics for 10-m Wind Speed, 2-m Temperature, and 2-m Relative Humidity
967 for a fog and clear sky case.

		10-m Wind Speed		2-m Temperature		2-m Relative Humidity	
		BACM	**UACM**	**BACM**	**UACM**	**BACM**	**UACM**
Fog Event Case [29-30 January 2017]	**IOA**	0.76	**0.89**	0.9	**0.96**	0.91	**0.92**
	MB	0.52	**0.14**	-1.03	**0.13**	**-1.32**	-6.62
	NMB	0.38	**0.09**	-0.06	**0.009**	**-0.01**	-0.07
	ME	0.69	**0.36**	2.0	**1.17**	**6.62**	7.49
	NME	0.48	**0.24**	0.13	**0.07**	**0.07**	0.08
	RMSE	0.9	**0.46**	2.29	**1.41**	**9.21**	9.33
Clear Sky Case [20-22 Dec 2016]	**IOA**	0.62	**0.88**	0.93	**0.94**	**0.76**	0.7
	MB	1.04	**0.18**	**0.7**	1.48	**-16.57**	-20.5
	NMB	0.33	**0.05**	**0.04**	0.08	**-0.24**	-0.3
	ME	1.13	**0.38**	1.7	**1.58**	**16.6**	20.5
	NME	0.35	**0.11**	0.1	**0.09**	**0.24**	0.3
	RMSE	1.39	**0.48**	2.05	**1.79**	**19.25**	22.1

968 Note: BACM = Base Asymmetric Convective Model; UACM = Urban Asymmetric Convective
969 Model; IOA = Index of Agreement; MB = Mean Bias; NMB = Normalized MB; ME = Mean
970 Error, NME = Normalized ME; RMSE = Room-Mean-Square Error.

971

972

973